LBNL Report Number LBNL-60008

Dynamic Molecular Imaging of Cardiac Innervation Using a Dual Head Pinhole SPECT System

Jicun Hu, Rostyslav Boutchko, Arkadiusz Sitek,
Bryan W. Reutter, Ronald H. Huesman, Grant T. Gullberg

E. O. Lawrence Berkeley National Laboratory,
Life Science Division
Berkeley, CA

Abstract – **Typically ^{123}I-MIBG is used for the study of innervation and function of the sympathetic nervous system in heart failure. The protocol involves two studies: first a planar or SPECT scan is performed to measure initial uptake of the tracer, followed some 3-4 hours later by another study measuring the wash-out of the tracer from the heart. A fast wash-out is indicative of a compromised heart. In this work, a dual head pinhole SPECT system was used for imaging the distribution and kinetics of ^{123}I-MIBG in the myocardium of spontaneous hypertensive rats (SHR) and normotensive Wistar Kyoto (WKY) rats. The system geometry was calibrated based on a nonlinear point projection fitting method using a three-point source phantom. The angle variation effect of the parameters was modeled with a sinusoidal function. A dynamic acquisition was performed by injecting ^{123}I-MIBG into rats immediately after starting the data acquisition. The detectors rotated continuously performing a 360° data acquisition every 90 seconds. We applied the factor analysis (FA) method and region of interest (ROI) sampling method to obtain time activity curves (TACs) in the blood pool and myocardium and then applied two-compartment modeling to estimate the kinetic parameters. Since the initial injection bolus is too fast for obtaining a consistent tomographic data set in the first few minutes of the study, we applied the FA method directly to projections during the first rotation. Then the time active curves for blood and myocardial tissue were obtained from ROI sampling. The method was applied to determine if there were differences in the kinetics between SHR and WKY rats and requires less time by replacing the delayed scan at 3-4 hours after injection with a dynamic acquisition over 90 to 120 minutes. The results of a faster washout and a smaller distribution volume of ^{123}I-MIBG near the end of life in the SHR model of hypertrophic cardiomyopthy may be indicative of a failing heart in late stages of heart failure.**

This work was supported in part by grants R01EB00121 and R01HL50663 from the National Institutes of Health (NIH), and the U.S. Department of Energy under Contract No. DE-AC03-76SF00098

Rostyslav Boutchko, Bryan W. Reutter, Ronald H. Huesman, and Grant T. Gullberg are with the Department of Medical Imaging Technology, Lawrence Berkeley National Laboratory, Berkeley, CA, 94720, USA. Telephone: (510) 486-7483 Email: gtgullberg@lbl.gov

Jicun Hu was with LBNL but is presently at Siemens Medical Systems, Knoxville, TN.

Arkadiusz Sitek was with LBNL but is presently at Harvard Medical School, Department of Radiology, Brigham and Women's Hospital, Boston, MA

I. INTRODUCTION

Single Photon Emission Computed Tomography (SPECT) is an important diagnostic tool for investigating organ function in health and disease. In addition to being a useful diagnostic tool in humans, it is also an important tool to follow the progression of disease in small animals. Of particular interest is the use of the spontaneous hypertensive rat (SHR) model to follow the progression of heart failure in hypertrophic cardiac myopathy. One aspect that is manifested in heart failure is changes in sympathetic neuronal function. In this work a clinical pinhole SPECT scanner is used to image ^{123}I-MIBG in the SHR model to ascertain changes in neuronal function with the progression of congestive heart failure. Pinhole SPECT has been widely used to image small animals in the study of physiological processes because of its capability to achieve good spatial resolution, which is very desirable in imaging small objects (Palmer 1990, Metzler 2005a, Beekman 2005). SPECT imaging is usually performed to measure static tracer distribution, however, it is hypothesized that dynamic SPECT imaging will provide a more sensitive measure of changes in neuron function with progression of heart failure in the SHR model.

In this work we use the SHR model to study changes in sympathetic innervation with the progression of hypertrophy. The SHR (Okamoto and Aoki Strain) has hypertension associated with generalized dyslipidemia and insulin resistance. It has been noted that CD36 is a defective gene on chromosome 4 (Hajri 2001). The gene contains multiple sequence variants, that in the SHR results in a defective fatty acid translocase, which functions in long chain fatty acid transport into the cell. This compromises tissue utilization of fatty acid and increases the basal glucose metabolism and hyperinsulinemia. A high rate of glucose uptake increases insulin requirement and over expression of the membrane protein glut1 results in eventual insulin resistance. A short chain fatty acid supplement diet decreases glucose uptake and alleviates hypertrophy, but hypertension is not improved. Since increased glucose oxidation is essential in pressure-overload hypertrophy, decreased glucose transport into the myocyte may play a role in contractile dysfunction in the failing heart. A valuable aspect of studies in the SHR is that long-term studies over the course of its two year lifespan are feasible.

The sympathetic nervous system plays a crucial role in the development and progression of heart failure in patients with reduced left ventricular systolic function (O'Keefe 2000). Patients with heart failure have elevated levels of circulating catecholamines that increase in proportion to the severity of heart failure (Bristow 1997, Esler 1997). Acute adrenergic stimulation of the myocardium causes increases in heart rate, contractility, and conduction, thereby temporarily increasing cardiac output. However, chronic excessive sympathetic nervous system stimulation

causes myocardial toxicity and further depression of left ventricular systolic function (Eichhorn 1996, Bristow 1997, Esler 1997). The SHR model has been used to study adrenergic neuron remodeling in congestive heart failure (Sisson 1991). The SHR model exhibits more aspects that are indicative of diastolic dysfunction. However, this is not clear; we will show in this report that the SHR may have a faster washout toward the end of life, which could be the result of the downregulation of the sympathetic nervous system which in turn results in systolic dysfunction.

The cardiac autonomic nervous system consists of both sympathetic and parasympathetic innervation (Bengel 2004). Each system differs in their major neurotransmitters. The primary sympathetic transmitter is norepinephrine and the primary parasympathetic transmitter is acetylcholine; each exhibit stimulating or inhibitory effects in target tissues via adrenergic and muscarinic receptors, respectively. Norepinephrine is synthesized and stored within vesicles of the neurons. Neuronal stimulation leads to norepinephrine release through exocytosis. Release is regulated by a number of presynaptic receptor systems. Most of the norepinephrine released from the presynaptic neuron undergoes reuptake by the energy dependent norepi transporter (NET-1) mechanism and recycles into vesicles, or is metabolized in the cytosol, and only a small amount of released norepinephrine actually activates postsynaptic receptors on the surface of the myocyte. When prolonged excessive stimulation of adrenergic receptors takes place, the first consequence is desensitization of adrenoceptors, followed by down regulation with enhanced receptor degradation and decreased receptor synthesis. The next step is downregulation of adenylyl cyclase, which results in decreased myocardial reserve and impaired exercise capacity.

Metaiodobenzylguanidine (MIBG) is a functional analog of norepinephrine and is thought to share the same uptake, storage, and release mechanisms as norepinephrine in the nerve terminals but is not metabolized (Wieland 1981a, Nakajo 1986, Pissarek 2002, DeGrado 1995, Glowniak 1993,Guilloteau 1984, Carrio 2001, Dae 1995). ^{123}I-MIBG is used to assess the innervation of the sympathetic nervous system in the heart. The distribution of ^{123}I-MIBG most closely depicts the distribution of sympathetic neurons, and provides an accurate depiction of myocardial sympathetic innervation and allows a unique characterization of alterations in regional sympathetic nerve function (Dae 1995). ^{123}I-MIBG has been used in several clinical studies (Dae 1995, Mitrani 1993, Gill 1993, Maunoury 2000, Henderson 1988, Nakajima 1994, Tomaselli 1994, Lotze 2001). Cardiac ^{123}I-MIBG uptake and washout predicts outcome more effectively than any of the standard noninvasive measurements of left ventricular function in patients with congestive heart failure (CHF). Clinically, ^{123}I-MIBG is used in the diagnosis of heart failure (CHF, dilated cardiomyopathy, hypertrophic cardiomyopathy), evaluation of neuronal function after heart transplant, evaluation of heart function with diabetes and during

chemotherapy, and in the evaluation of arrhythmias. A high washout rate means increased adrenergic activity (Patel 2002). SHRs seem to develop similarities to patients with heart failure. They develop a generally enhanced sympathetic tone and a downregulation of cardiac receptors (Pissarek 2002, Dubois 1996, Bohlender 2000). In our work a 2-compartment model was used to model the kinetics of ^{123}I-MIBG. The effect of alterations of the supracardiac receptor population for cardiac norepinephrine turnover, the density or activity of uptake-1 transporters, and the perfusion of cardiac microcompartments is not fully understood (Pissarek 2002).

Small-animal imaging studies associated with molecular imaging are rapidly growing (Massoud 2003, Weissleder 2001). Nuclear imaging of small animals involves the use of microPET (Cherry 2001), microSPECT (a dedicated small animal system) (McDonald 2000, McElroy 2002, Furenlid 2004, Beekman 2004, Meikle 2005, Goertzen 2005, Beekman 2005, Kim 2006, Zeniya 2006, Hesterman 2007, Vastenhouw 2007), and pinhole SPECT technologies (Strand 1993, Weber 1994, Strand 1994, Jaszczak 1994, Li 1995a, Weber, 1995, Ishizu 1995, Yukihiro 1996, Smith 1997a, Smith 1998, Ogawa 1998, Tenney 1999, Wu 1999, Wu 2000, Hirai 2000, Hirai 2001, Acton 2002a, Acton 2002b, Wu 2003, Schrammm 2003, Metzler 2004, Zimmerman 2004, Vanhove 2005, Metzler 2005a, Zhou 2005, Acton 2006, Ostendorf 2006, Forrer 2006). For reviews of small animal imaging of single photon tracers see (Budinger 2002, Weber 1999, Peremans 2005, Beekman 2007). Some of the microSPECT systems use modified commercial clinical systems in which the camera does not rotate but a special collimator insert is provided for small animal imaging (Beekman 2004, Beekman 2005, Vastenhouw 2007), or the animal is rotated in front of a fixed gamma camera (Habraken 2001, Booij 2002, de Win 2004, Andringa 2005). Many of the newer designs are looking to use new CZT technology (Liu 2002, Kim 2006, Hesterman 2007) as opposed to older NaI detector technology. Pinhole SPECT (in our classification) differs from a microSPECT system in that it uses pinhole collimators with a large field of view clinical SPECT/CT system. The use of pinhole SPECT/CT technology allows for the more direct translation of development in small animal models to clinical application where SPECT/CT technology is most applicable. Other pinhole SPECT systems have been used to image the heart (Yukihiro 1996, Wu 1999, Wu 2000, Hirai 2000, Hirai 2001, Wu 2003, Vanhove 2005, Zhou 2005, Acton 2006) (commercial patient SPECT systems) and dedicated small animal microSPECT systems (Coaanstantinesco 2005, Beekman 2005, Liu 2002).

Our work builds on excellent theoretical work of others (Li 1994, Li 1995b, Wang 1996, Smith 1997b, Smith 1997c, Smith 1998b, Metzler 2001, Metzler 2002, Metzler 2003, Zeniya 2004, Sohlberg 2004, Meng 2004, Bal 2006, Hsu 2006, Rentmeester 2007). The two-detector GE Millennium VG3 SPECT/CT system at LBNL which we use to develop a pinhole SPECT

technique directed toward cardiovascular imaging of rats, is a SPECT/CT clinical system used for patients. This differs from the dedicated small animal SPECT/CT systems and our x-ray CT resolution is not as good as that of the dedicated small animal systems. SPECT imaging of small animals can be performed on commercial clinical imaging systems with specially designed pinhole collimators. A resolution on the order of 1 mm can be obtained in mice (Ogawa 1998) with ^{99m}Tc agents and with cardiac gating for heart rates as high as 400 beats per minute (Wu 1999, Wu 2000). Combining a low-energy isotope with gold alloy pinholes allows for a resolution of a few hundred m in mice (Beekman 2002). Our investigation allows for the study of mechanisms and treatment of human diseases in animal models and permits longitudinal investigations that track physiologic changes over time in the same animal. The evaluation of radiopharmaceuticals in small animals can be a tremendous asset for the translation to the clinic. For example, at present, GE Healthcare is evaluating ^{123}I-MIBG for imaging heart failure. We expect that our work with small animals using ^{123}I-MIBG, will develop new technology in terms of data acquisition techniques and algorithms for processing ^{123}I-MIBG imaging data which will directly be appropriate for clinical application.

It is well known that a pinhole SPECT system is very sensitive to geometrical misalignment because of the magnification effect. The trajectory of the pinhole for our SPECT system is a circle within a plane. Seven parameters are enough to characterize the geometry of the imaging system if the geometrical parameters do not change from view to view (Noo 2000, Beque 2003). However, due to variations in the gravitational torque of the detector as a function of angle, we found that some parameters change with the view angle. In particular, we found that the axial and transaxial mechanical shift has a sinusoidal variation as a function of angle. Also, since the SPECT system has two detector heads, we model the axial difference between the two-pinhole collimators. A nonlinear least square fitting method is applied to obtain the parameters for the imaging geometry (Gullberg 1987, Beque 2003). Our calibration procedure obtains good fits to the measured projections of the point sources.

In this work we perform dynamic pinhole SPECT imaging using ^{123}I-MIBG. MIBG is taken up by sympathetic nerves in a manner similar to norepinephrine, but is not metabolized. The distribution of MIBG closely depicts the distribution of sympathetic neurons and provides an accurate depiction of myocardial sympathetic innervation. In so doing it allows a unique characterization of alterations in regional sympathetic nerve function (Sisson 1987, Dae 1995, Carrio 2001, Patel 2002). MIBG has been widely used in clinical studies to provide diagnostic information for the cardiac sympathetic innervation (Nakajima 1994, Maunoury 2000). Faster

MIBG washout rate in the heart, which reflects accelerated cardiac adrenergic neuronal activity, is indicative of a compromised heart (Henderson 1988, Arimoto 2004).

Because of the fast blood circulation and slow camera rotation it is difficult to estimate an input function from the dynamic data. Factor analysis (FA) is a semi-automatic tool used to extract TACs for different organs with different kinetics (Barber 1980). It can be applied to dynamically acquired projections (Sitek 2001) or a dynamic sequence of reconstructions (Sitek 2000). For the dataset we collected, the initial injected bolus travels throughout the vascular system too fast to obtain a consistent set of projections for the first 90 second rotation; therefore, a tomographic reconstruction for the first rotation is not appropriate. To obtain the input function for compartmental modeling, we applied the FA method directly to the projections. Starting with the second rotation, the projections become relatively consistent and we applied the ROI sampling method to the dynamic sequence of reconstructions. These two types of TACs can be connected since the same system matrix is used for the direct FA on projections and for the iterative reconstruction of the ROIs. The TACs for the myocardium and blood pool are then fit to two-compartment model .

This paper is organized as follows. The materials and methods for this work are described in section II. We introduce calibration and reconstruction methods for the dual head pinhole SPECT system. The kinetic analysis method for the dynamic data is also presented. The pinhole SPECT calibration and image reconstruction results are presented in section III. Also in this section, we provide the results for kinetics analysis. Finally, conclusions and discussions are provided in section IV.

II. MATERIALS and METHODS

A. Dual Head Pinhole SPECT System

Our pinhole SPECT system, shown in Fig. 1, was set up by mounting two pinhole collimators (Nuclear Fields, Vortum-Mullen, The Netherlands) on a GE Millennium VG3 dual head SPECT system with slip ring detector technology. The 45 cm × 45 cm detectors each have a crystal thickness of 3/8 inches, providing an intrinsic spatial resolution of 3.9 mm and energy resolution of 9.8% at an energy of 140 keV. The pinhole collimators had a focal length of 25 cm and allowed for pinhole inserts of different sizes. In our work we used a tungsten insert with a 1.5 mm aperture. The magnification (ratio between pinhole to detector distance and pinhole to rotation axis distance) using our pinhole SPECT system to image a rat was approximately 5. The data were acquired using a circular trajectory. Although the circular planar orbit does not provide complete data for cone beam tomographic acquisition, we found it to be adequate for our cardiac imaging for the following three reasons: first, the cone angle involved is relatively small; second, there is some axial displacement (4-5 mm) between the two pinholes, which increases the data sampling completeness; and third, the heart does not extend very far from the central plane of the cone beam geometry.

Figure 1. Pinhole SPECT scanner used for the dynamic cardiac data acquisition in a rat.

B. Calibration of the Dual Head Pinhole System

Since the pinhole system is very sensitive to geometrical misalignment, it is important to accurately estimate the geometric parameters to obtain an accurate system matrix, which will be used in the reconstruction. We calibrated our dual head pinhole SPECT system using a nonlinear

point projection fitting method first proposed in (Gullberg 1987) and later in (Hsieh 1992). For a pinhole SPECT system with a circular planar orbit, it was shown in (Beque 2003) that the projections of 3 point sources separated by a known distance from each other is enough to obtain a unique solution for the 7 parameters needed to fully characterize the geometry of a circular planar orbit pinhole SPECT system, assuming that the parameters remain unchanged over the entire rotation. Figure 2 shows an illustration of our dual head pinhole SPECT system. For our SPECT system, we found that because the detector heads extend from the gantry (Fig. 1) they produce a moment arm that varies as the detectors rotate around the bed, causing the heads to slightly shift axially (Fig. 3). Also, we model the transaxial mechanical shift as an angle variant, which may be caused by the imperfectness of the gantry. We estimate these shifts as sinusoidal functions of view angle. Finally, the initial axial distance between the two pinholes is included in the calibration procedure.

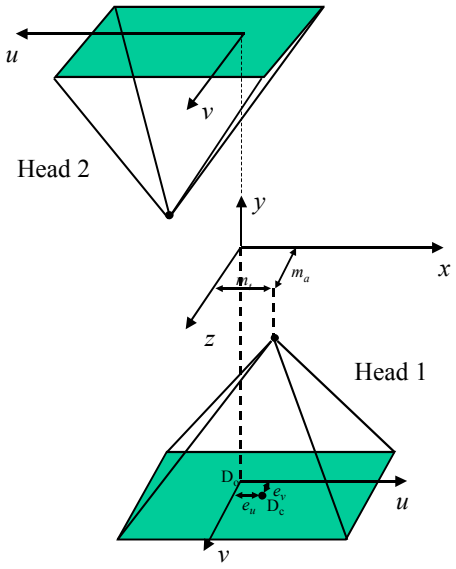

Figure 2. Illustration of dual head pinhole SPECT system and geometrical parameters.

The tilting of the detector heads as a function of view angle causes several effects. First, it causes the tilt angle of the gamma detector to change; second, it causes the distance of the pinhole to the rotation axis to change; and third, it causes the axial pinhole location to change as a function of angle. One challenge exists for accurately modeling the tilting angle variation: it is difficult to determine the location of the rotation axis of the gamma camera. Figure 4 shows that the detector tilting angle can change around the two different fulcrums. In each case, the view angle dependent parameters have to be modeled differently, which complicates the calibration task. However, we can show that if the amplitude of the radius and tilt angle change is very small,

it will cause very little effect on the image reconstruction. The change of axial location of the pinhole plays a major role in obtaining the final image reconstruction. Therefore, in the calibration, we only model the axial change of the pinhole aperture with different view angles while keeping the tilt angle and the distance from the pinhole to axis of rotation constant. We found that this simplification gives us satisfactory results in the calibration. Table 1 summarizes the geometrical parameters we need to estimate for each pinhole detector. Refer to (Metzler 2005b) for a good understanding of mechanical shift and electronic shift.

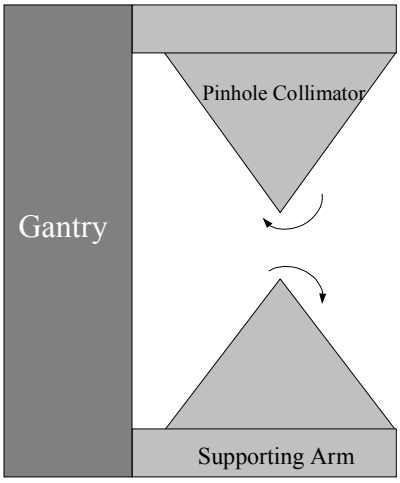

Figure 3. Axial view of the dual head pinhole SPECT system, which illustrates the axial shift of the pinholes.

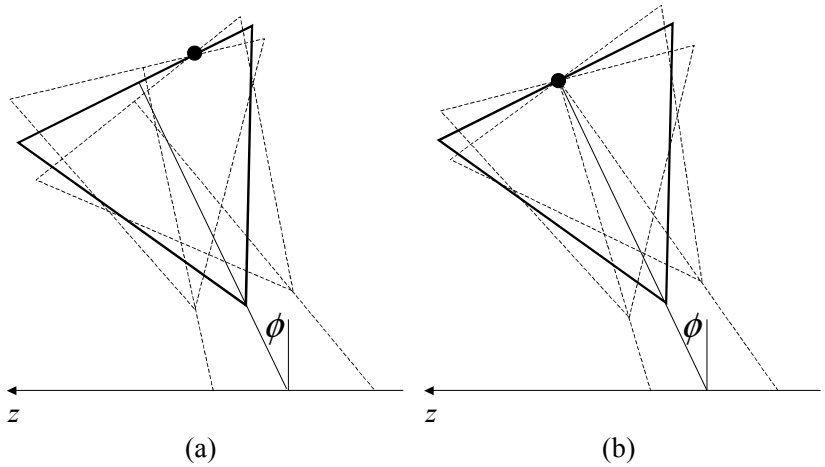

Figure 4. Illustration of the detector tilting around two different fulcrums. (a) Illustrates rotation off axis and (b) illustrates rotation on axis. The angle of tilt is exaggerated for the illustrations. The angle tilt is very small (less than 1°) in our pinhole SPECT system.

Geometrical parameters	Mathematical notations
Pinhole to rotation axis distance	d
Pinhole to detector distance	f
Transaxial mechanical shift	$m_t(\theta)$
Axial mechanical shift	$m_a(\theta)$
u electronic shift	e_u
v electronic shift	e_v
Tilt angle	ϕ
Twist angle	ψ

Table 1. Geometrical parameters for a single pinhole SPECT system, θ represents the view angle, mechanical shift and tilt angle is modeled as a function of angle.

The transaxial mechanical shift of detector head *h* (*h=1,2*) as a function of view angle is modeled as

$$(m_t(\theta))_h = (m_{t_d})_h + (m_{t_s})_h \sin\theta + (m_{t_c})_h \cos\theta \quad , \tag{1}$$

where $(m_{t_d})_h$ is the DC component of the transaxial mechanical shift of head *h*, $(m_{t_s})_h$ is the coefficient of the *sin* component, and $(m_{t_c})_h$ is the coefficient of the *cos* component.

The axial mechanical shift of detector head *h* (*h=1,2*) as a function of view angle is modeled as

$$(m_a)_h = (m_{a_d})_h + (m_{a_s})_h \sin\theta + (m_{a_c})_h \cos\theta + (m_{a_{init}})_h \,, \tag{2}$$

where we set $(m_{a_d})_h = -(m_{a_c})_h$, so that when $\theta = 0$, $(m_a)_h = (m_{a_{init}})_h$; $m_{a_{init}}$ is the initial axial location of the pinhole, when $\theta = 0$; and we assume $(m_{a_{init}})_1 = 0$ and $(m_{a_{init}})_2 = \Delta z$ **,** where Δz is the initial axial difference between the two pinholes.

From the above, we see that 12 parameters (3 each for transaxial mechanical shift and axial mechanical shift) are estimated for each head. Since we assume that $(m_{a_{init}})_1 = 0$, a total of 23 parameters need to be estimated for the dual head pinhole SPECT system. It should be noted that the shift of the geometrical parameters as a function of angle have also been studied in (Crawford 1988, Beque 2004, Metzler 2005c).

The calibration phantom illustrated in Fig. 5 was used to estimate the geometric parameters. Point sources (small beads soaked with ^{99m}Tc) were placed at five locations shown in Fig. 5. The phantom was placed on the support holder for the rats and 120 projections were collected using a step and shoot acquisition mode and each projection were acquired for 18 seconds. After projections were collected from different view angles, the geometrical parameters were estimated by minimizing the following chi-square equation:

$$\chi^2 = \sum_h \sum_i \sum_\theta \left[(u_{i,\theta,h}^{img} - u_{i,\theta,h}^{est})^2 + (v_{i,\theta,h}^{img} - v_{i,\theta,h}^{est})^2 \right] \quad , \tag{3}$$

where h is the index of the detector heads, i is the index for the points in the object space, θ is the index of the view angle, $(u_{i,\theta,h}^{img}, v_{i,\theta,h}^{img})$ is the coordinate of the measured centroid of the projection of the point source, and $(u_{i,\theta,h}^{est}, v_{i,\theta,h}^{est})$ is the estimated coordinate of the projected centroid, which is a function of the geometrical parameters and the point source location. Axially, the initial location of the first head was used as a reference.

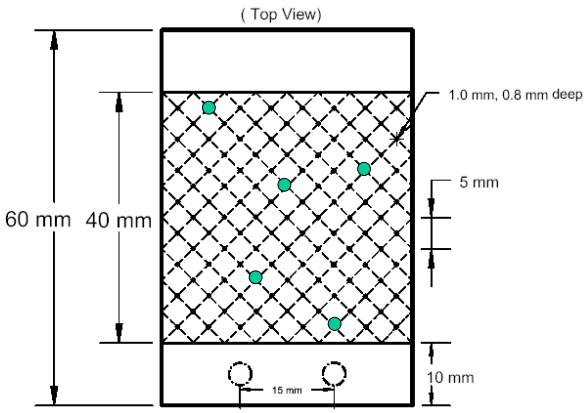

Figure 5. Illustration of the calibration point source phantom. (Supplied to us by Benjamin Tsui, Ph.D., Johns Hopkins University)

In the following, we illustrate how to calculate the projections $(u_{i,\theta,h}^{img}, v_{i,\theta,h}^{img})$ of point sources onto the detector heads at different view angles as a function of the geometrical parameters and location of point sources: (x_i, y_i, z_i) $i = 1,2,3$. The projections $(u_{i,\theta,h}^{est}, v_{i,\theta,h}^{est})$ in Fig. 6 are calculated as follows:

$$u_{i,\theta,h}^{est} = f_h \frac{m_{\theta,h}\cos\psi_h - x_i^r(\theta_h,\phi_h,\psi_h)}{d_h + y_i^r(\theta_h,\phi_h,\psi_h)} + m_{\theta,h}\cos\psi_h + e_{u,h} \quad , \tag{4}$$

$$v_{i,\theta,h}^{est} = f_h \frac{m_{\theta,h}\sin\psi_h - z_i^r(\theta_h,\phi_h,\psi_h)}{d_h + y_i^r(\theta_h,\phi_h,\psi_h)} + m_{\theta,h}\sin\psi_h + e_{v,h} \quad , \tag{5}$$

where (x_i^r, y_i^r, z_i^r) is calculated as follows:

$$\begin{bmatrix} (x_i^r)_h \\ (y_i^r)_h \\ (z_i^r)_h \end{bmatrix} = \begin{bmatrix} \cos\psi_h & 0 & -\sin\psi_h \\ 0 & 1 & 0 \\ \sin\psi_h & 0 & \cos\psi_h \end{bmatrix} \begin{bmatrix} 1 & 0 & 0 \\ 0 & \cos\phi_h & -\sin\phi_h \\ 0 & \sin\phi_h & \cos\phi_h \end{bmatrix} \begin{bmatrix} \cos\theta_h & \sin\theta_h & 0 \\ -\sin\theta_h & \cos\theta_h & 0 \\ 0 & 0 & 1 \end{bmatrix} \begin{bmatrix} x_i \\ y_i \\ z_i \end{bmatrix} + \begin{bmatrix} 0 \\ 0 \\ (m_a(\theta))_h \end{bmatrix} \tag{6}$$

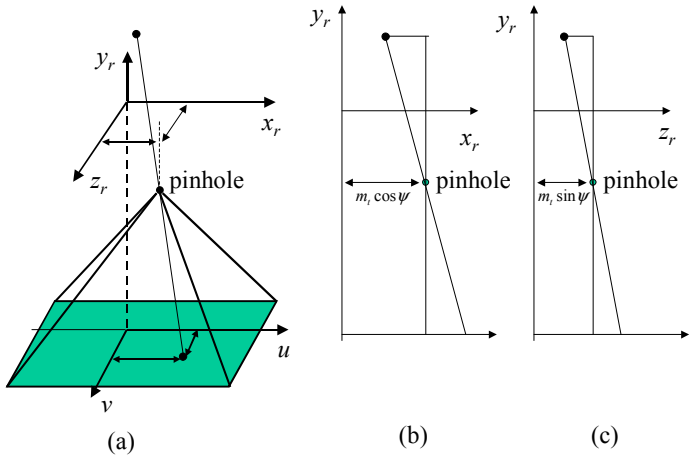

Figure 6. Illustration of $(u_{i,\theta,h}^{est}, v_{i,\theta,h}^{est})$. (a) The 3D perspective of projection of a point source through the pinhole. (b) 2D illustration of the calculation of the coordinate $u_{i,\theta,h}^{est}$. (c) 2D illustration of the calculation of the coordinate $v_{i,\theta,h}^{est}$.

The geometrical parameters of both heads and the 3D coordinates of the point sources are estimated by minimizing equation (3).

C. Reconstruction of Data Acquired with the Dual Head Pinhole System

System matrix. The dual head pinhole SPECT data acquisition can be modeled in the following affine transformation:

$$\overline{P} = \alpha x + r \quad , \tag{7}$$

where $P \in R^{M\times 1}$ is the expectation of the detected data, $x \in R^{N\times 1}$ is the unknown tracer distribution, $\alpha \in R^{M\times N}$ is the system matrix with the (*i*,*j*)th element containing the probability of detecting an event from image voxel j at detector pixel i, and r is the noise. M is the number of detector elements for both heads and N is the number of image voxels. Although various types of basis functions exist, we chose cubic voxels for this work because of their simplicity.

Since emission data is very noisy, iterative methods that properly account for the Poisson statistics are usually applied to obtain image reconstruction. The system matrix, which describes the photon detection physics, plays a very important role in almost all iterative reconstruction algorithms. In the following, we describe how to calculate α_{ij}, which is the probability of detecting a photon emitted from voxel *j* in detector *i*, ignoring the effects of attenuation and scatter, for a pinhole SPECT system.

Figure 7 shows the geometry for how the activity from voxel *j* is detected by a detector bin *i* through the pinhole system. Assume there is a unit of activity within voxel *j*, then the fraction of activity from voxel *j,* which will be detected in pixel *I,* is calculated as follows:

$$F = \frac{A_j \times d}{V_j} \quad , \tag{8}$$

where A_j is the area of intersection (represented by the thick solid line in the voxel) of the inverse cone subtended by the pinhole and the detector pixel with the voxel; *d* is the length of the voxel side; and V_j is the volume of voxel *j*. The area A_j is given by

$$A_j = \frac{h^2}{f^2} \times A_p \quad , \tag{9}$$

where A_p is the area of the detector pixel and the length *d* is given by

$$d = l(i,j)\cos\theta \quad , \tag{10}$$

where *l* is the length of the line connecting the center of the pixel and the center of the voxel *j* and θ is the angle between the horizontal line and the line connecting the centers of pixel *i* and voxel *j*. Substituting equation (9) and equation (10) into equation (8), gives the following expression for the fraction of activity from voxel *j,* which will be detected in pixel *i*

$$F = \frac{h^2}{V_j f^2} \times A_p \times l(i,j) \cos\theta \quad . \tag{11}$$

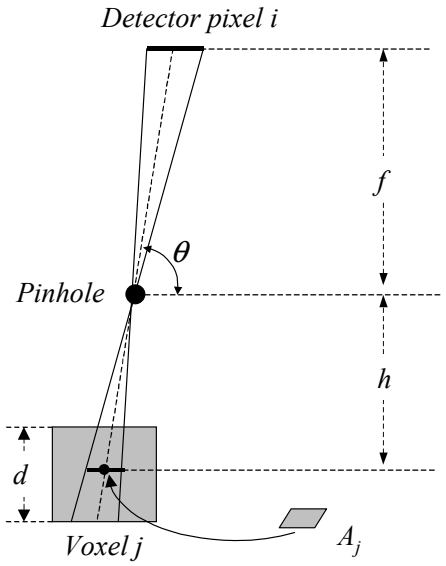

Figure 7. Geometry of pinhole detection.

From (Anger 1959), the geometrical sensitivity of the pinhole camera is

$$\begin{aligned} Sens(\theta) &= \frac{\pi \times r \times (r \sin\theta)}{4\pi (h/\sin\theta)^2} \\ &= \frac{r^2 \sin^3\theta}{4h^2} \end{aligned} \tag{12}$$

where r is the radius of the pinhole.

Therefore, the activity emitted from voxel *j,* which will be detected in detector *i,* is as follows,

$$\begin{aligned} \alpha(i,j) &= F \times sens(\theta) \\ &= \frac{r^2 \sin^3\theta}{4h^2} \times \frac{h^2}{V_j f^2} \times A_p \times l \sin\theta \quad . \\ &= \frac{r^2 A_p}{4 V_j f^2} l(i,j) \sin^4\theta \end{aligned} \tag{13}$$

The results are similar to that derived in (Li 1995b). Attenuation and scatter, which may be minor, is not compensated for in the current implementation.

Model for the point spread function. There are different methods to compensate for the point spread function because of the finite size of the pinhole aperture. We applied a multi-ray

technique, which is illustrated in Fig. 8. We subdivide both detector pixels and pinhole aperture into multiple sub-elements and form multiple lines by connecting each sub-element in the detector pixel with those in the pinhole aperture. Using the multi-ray model, the septum penetration effect is easily modeled as long as the geometry of the septum is known.

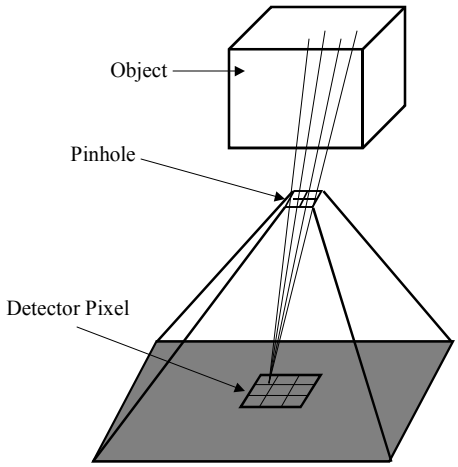

Figure 8. Model for point spread function using a multi-ray technique.

Reconstruction algorithm. After the system matrix is obtained for the dual head pinhole SPECT system, different iterative algorithms can be applied to obtain the image reconstruction. In this work, we applied the ML-EM algorithm to obtain the image reconstruction. All images of 80×80×80 (0.85 mm) were reconstructed from 128×128 (4.42 mm) projections using 30 iterations of the ML-EM algorithm. A Gaussian filter with kernel [0.458 1 0.458] was applied to obtain the final images. The system matrix was pre-calculated and stored. The point spread function was modeled by a multi-ray technique. The effect of attenuation and scatter was not modeled in the reconstruction procedure. However, since the algorithm is ray driven, attenuation compensation can easily be incorporated into the reconstruction as long as an attenuation map is available. A computation time of 2 hours was required to obtain a reconstruction.

D. Dynamic Imaging Protocol

Two groups of rats were involved in the dynamic imaging of cardiac innervation (Table 2). Each group contained one control WKY rat and one SHR . The study was approved by our Animal Welfare and Regulatory Committee. The weights of the rats were measured before they were imaged. Four studies were performed over eight months up until the death of one of the SHR's, at which time we sacrificed the other three rats and performed histology on all four rats.

In each study, the rats were scanned according to the dynamic scanning protocol described below. Pinhole collimators of a focal length of 25 cm with an aperture diameter of 1.5 mm were mounted on our pinhole SPECT system (Fig. 1). The energy window was set at 20% centered on 159 keV. The rats were anesthetized with 2% isofluorene and oxygen and positioned in a support holder mounted on the patient bed. A dynamic acquisition was performed by injecting 5 mCi of ^{123}I-MIBG (half life of 13 hrs) into the rat immediately after starting the data acquisition. The detectors rotated continuously performing a 360° data acquisition every one and half minutes. For each rotation, 90 1-second 128×128 projections of 4.42 mm pixels were acquired. A total of 66 rotations of data acquisition were obtained. We also measured the systolic pressure of the rats at 4/19/05, which showed that the hypertensive rats had higher blood pressure than that of the normal rats.

Date	Group	Rat Type	Weight (grams)	Study Type	BL Press (mm Hg)
03/02/05	1	WKY	472	Dynamic	
		SHR	440	Dynamic	
	2	WKY	465	Dynamic	
		SHR	458	Dynamic	
04/19/05					119
					164
					146
					169
05/17/05	1	WKY	506	Dynamic	
		SHR	443	Dynamic	
	2	WKY	492	Dynamic	
		SHR	458	Dynamic	
08/16/05	1	WKY	532	Dynamic	
		SHR	457	Dynamic	
	2	WKY	510	Dynamic	
		SHR	452	Dynamic	
11/29/05	1	SHR	406	Dynamic	
		WKY	572	Dynamic	
	2	SHR	426	Dynamic	
		WKY	505	Dynamic	

Table 2. Two groups of rats were studied at four separate times over a period of 8 months. All rats were born 5/08/04 (minus 84 days). In Group 1, the SHR died 1/01/06. The other three rats were sacrificed 1/05/06. The ratio of heart weight to total body weight was 0.64% SHR Group 1; 0.39% WKY Group 1; 0.59% SHR Group 2; 0.59% WKY Group 2.

E. Extracting Time Activity Curves from Dynamic Projections and Dynamic Reconstructions

The goal of this study was to explore the possibility of whether we could obtain kinetic parameters in the myocardium (washin and washout rates) from dynamically collected projections. The TACs in the myocardium tissue and blood pool are necessary for performing compartmental modeling to obtain the kinetic parameters, i.e. washin and washout rates, of the myocardial tissue. In order to extract TACs corresponding to blood pool and myocardium, we applied the FA method directly to the acquired projections to obtain the TAC for the blood pool for the first 90 seconds of the acquisition. Next, for the remainder of the data, we applied the ROI method on the dynamically reconstructed frames to obtain the TACs corresponding to the blood pool and myocardium. The ROIs were selected manually on the reconstructed summed image.

In the following, we describe the FA method applied directly to the projection data (Sitek 2001). This was applied to the data acquired for the first rotation of inconsistent projections to obtain the blood input function for this period. The factors F_{sk} and coefficients C_{ns} were estimated from the projection measurements $\hat{P}_m(k)$ by minimizing the following objective function:

$$f_{LS}(C,F) = \sum_{m,k=1}^{M,K} \frac{(\sum_{n,s=1}^{N,S} \alpha_{mn}(k) C_{ns} F_{sk} - \hat{P}_m(k))^2}{\hat{P}_m(k)} + f_{nneg}\,, \tag{14}$$

where $\alpha_{mn}(k)$ are the elements of the system matrix [as defined in equation (13)] describing the probability that photon emitted in voxel n was detected in projection bin m at projection k. The estimates for C and F are constrained by the non-negativity constraint:

$$f_{nneg}(C,F) = \sum_{n,s=1}^{N,S} \beta_c C_{ns}^2 U(-C_{ns}) + \sum_{k,s=1}^{K,S} \beta_F F_{sk}^2 U(-F_{sk})\,, \tag{15}$$

where U is a Heaviside function and $f_{nneg}(C,F)$ will penalize negative values for C_{ns} and F_{sk}. The strength of the penalty is controlled by positive parameters β_C and β_F. The variable S is the total number of factors, the variable K is the total number of projections, the variable M is the number of bins in each projection, and the variable N is the number of voxels.

The conjugate gradient algorithm (Press 1992) was used to minimize the least squares objective function in equation (14). The same system matrix was used here as in the reconstruction described in Section *C* above. The factor coefficients for two factors of 90 time

pointes were calculated for an 80×80×80 image matrix (0.85 mm voxels) from 90 1-second frames. The FA calculation required the conjugate algorithm to solve for 80×80×80×2+90×2=1024180 unknowns. It took about 10 days of computational time to solve for the factors and factor coefficients using a non-optimized code with a PowerPC G5 processor.

After the first rotation of 90 seconds, the projections were fairly consistent for the remaining 65 90-sec tomographic acquisitions. Therefore, ROIs were selected for the blood (~200 voxels) and for the myocardial tissue (~1800 voxels) and TACs were generated from the 65 dynamic reconstructions.

The FA suffers from the known problem of non-uniqueness (Sitek 2000). In order to constrain the solution we assumed that curves obtained from FA and curves obtained from ROI measurements should be connected without discontinuity. We forced the connection to be smooth by assuming that the values of *CF* obtained using direct FA were equal to the value in the reconstructed images at the point of connection since we used the same system matrix for direct FA and for the reconstructions.

The obtained TACs were corrected for radioactive decay according to the following equation:

$$M(t) = M(t)_{uncorrected} / 2^{-\frac{t}{T_{1/2}}} \tag{16}$$

where $T_{1/2}$ was the half-life of ^{123}I, which was 13 hours. Since the dynamic imaging procedure was about 1.5 hours, the radioactive decay accounted for less than 10% of the total decay, which included both radioactive and biological decay, for the entire duration of the imaging procedure.

F. Estimation for a Two-Compartment Model

After the TACs in the myocardium and blood pool were obtained, we fitted the curves to a two-compartment model (Fig. 2) to obtain the kinetic parameters. The TACs in the myocardium and the blood pool are defined by the following differential equations for a two-compartment model:

$$\frac{dM(t)}{dt} = K_{21} I(t) - K_{12} M(t)\,, \tag{17}$$

where $M(t)$ represents the TAC in the myocardium, $I(t)$ represents the TAC in the blood pool, and K_{21} and K_{12} are the wash-in and wash-out parameters, respectively.

When $M(0) = 0$, then the solution for equation (17) is

$$M(t) = K_{21} \int_0^t I(\tau) e^{-K_{12}(t-\tau)} d\tau\,, \tag{18}$$

when $M(0) \neq 0$, then the solution for equation (17) is

$$M(t) = K_{21}\int_0^t B(\tau)e^{-K_{12}(t-\tau)}d\tau + M(0)e^{-K_{12}t}. \quad (19)$$

The estimates for K_{21} and K_{12} can be determined by using a non-linear least squares fitting method, if $M(t)$ and $I(t)$ are known.

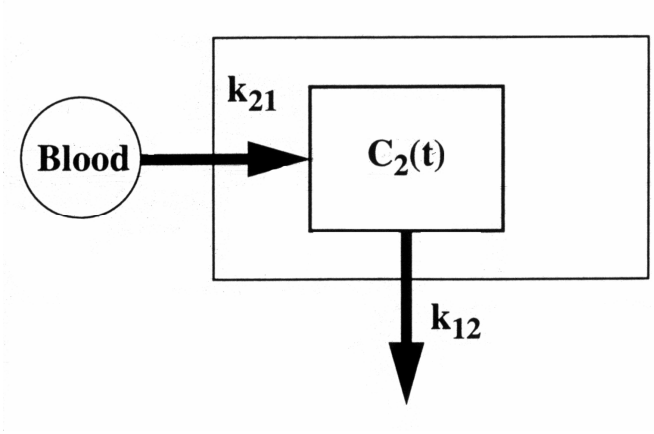

Figure 9. Two-compartment model. A two-compartment model was assumed in the washin and washout of 123I-MIBG from the presynaptic neurons of the sympathetic nervous system of the heart.

We also calculated the distribution volumes by taking the ratio of K_{21}/K_{12}. The distribution volume is illustrated in Fig. 10.

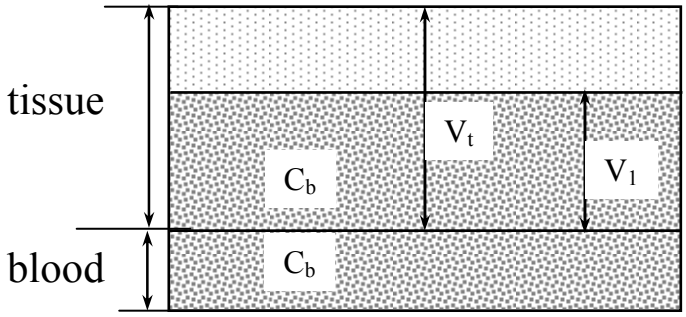

Figure 10. Distribution Volume. The distribution volume V_1 is the volume of tissue that would give the same tracer concentration as that in the blood. The distribution volume was calculated as K_{21}/K_{12}.

III. RESULTS

A. Calibration of the System Geometry

Projections of the 3 point sources (out of 5 point sources presented in Fig. 5) were obtained over a complete rotation of 360° for each detector. In the detector space, the projection of a point source travels along an ellipse. A non-linear least squares fitting method was applied to estimate the geometrical parameters. Table 2 presents the estimated parameters for one experiment. Figure 11 shows the comparison between the measured and the estimated centroids of the projected point sources. Geometrical parameters were modeled as a function of angle for the fits shown in Fig. 11(a), independent of angles for the fits shown in Fig. 11(b).

Geometrical parameters	Head 1	Head 2
Pinhole to rotation axis distance (mms)	55.3	57.9
Pinhole to detector distance (mms)	254.3	251.8
Transaxial mechanical shift (TMS) (DC component) (mms)	-0.79	-2.5049
Cosine component of TMS (mms)	-1.2851	-1.2850
Sine component of TMS (mms)	0.5587	0.0499
Initial Value of Axial Mechanical Shift (mms)	0	4.4819
Cosine component of AMS (mms)	1.8645	-1.9031
Sine component of AMS (mms)	0.2142	0.3433
u electronic shift (mms)	-0.5796	0.9622
v electronic shift (mms)	4.9031	-2.8271
Tilt angle (radians)	0.0194	-0.0030
Twist angle (radians)	-0.002	-0.0010

Table 3. Geometric parameters for one specific scanning experiment.

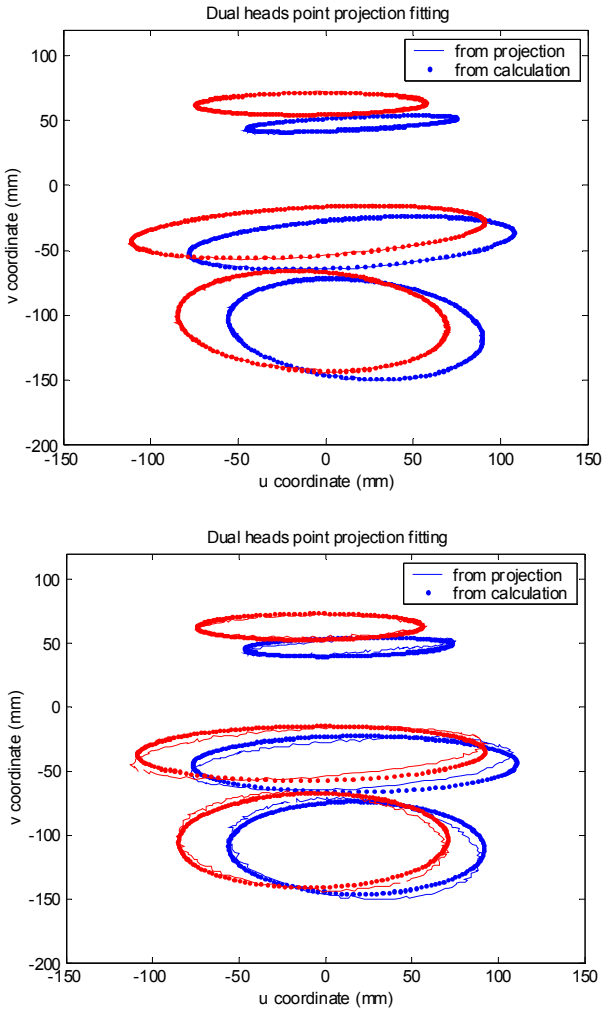

Figure 11. Nonlinear least square fits for the estimated centroids of the projected point sources. Geometrical parameters are assumed to be a function of angle in (a) and independent of angle in (b). The red plot is for head 1 and the blue plot is for head 2.

In order to test the performance of the calibrated pinhole SPECT system, we scanned and reconstructed a micro Jaszczak phantom. Figure 12 shows that the calibrated system has the capability to resolve the 1.2 mm rod sources.

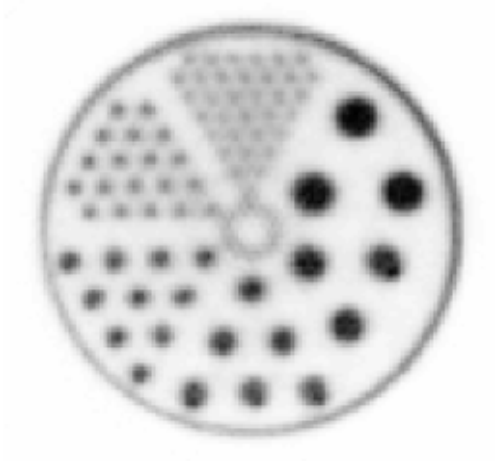

(a)

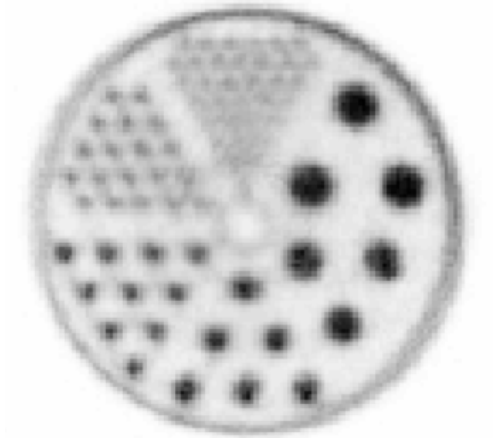

(b)

Figure 12. Reconstruction of a micro Jaszczak phantom. (a) Result for angle variant calibration. (b) Result for angle invariant calibration. The images are the sum of 40 0.85 cm reconstructed slices. The centers between the smallest sources are separated by 1.2 mm.

B. Dynamic Projections

Since the gantry cannot rotate fast enough to freeze the change of tracer activity within the heart, inconsistent projections are collected during the bolus input phase of the tracer. Keep in mind that the recirculation time in a rat is 8 seconds, whereas a complete set of projections are obtained every 90 seconds. Therefore, we observe in Fig. 13(a) that for the first rotation of data, the projections are not consistent as can clearly be seen because the distribution of the injection bolus changes during the first few projections and then seems to be more uniformly distributed in the blood and heart later on. After the first rotation the projections remain relatively consistent.

Figure 13(b) shows the relatively consistent projections on which a tomographic reconstruction can be performed.

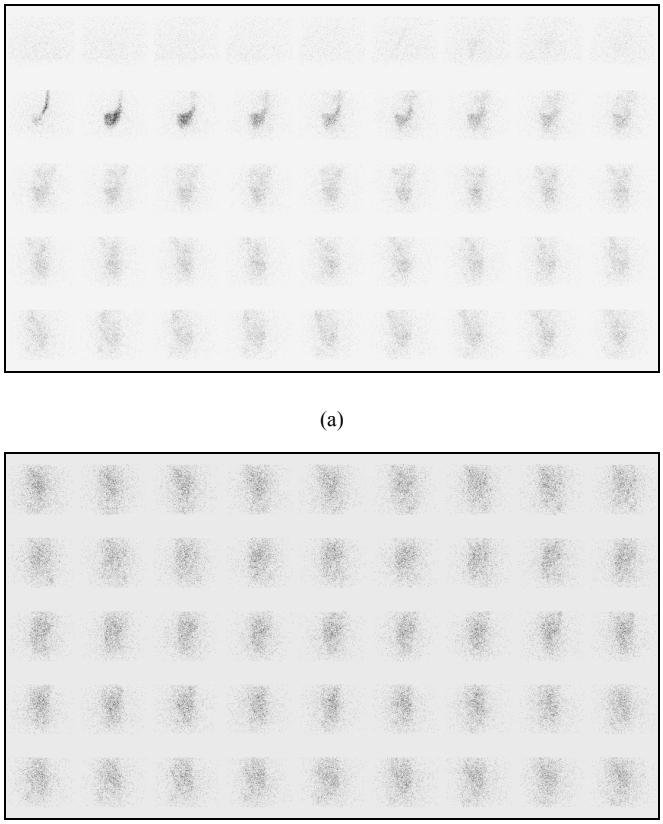

(a)

(b)

Figure 13. Dynamic projections. (a) First rotation of inconsistent projections. (b) Tenth rotation of relatively consistent projections.

C. Summed Static Reconstruction

Figure 14 shows volumetric reconstructions (36 slices) from summed events over 66 rotations of data for a control WKY rat. The images clearly show the distribution of ^{123}I-MIBG within the myocardium. It can be observed that ^{123}I-MIBG is also present in other organs, such as liver and spinal chord. The difference between the sympathetic and parasympathetic system is that sympathetic system innervates the heart directly from ganglia in the spinal cord, whereas the parasympathetic system innervates directly from regulatory centers in the midbrain, hypothalamus, pons, and medulla. However, these static reconstructions do not provide kinetic information, which is important in some circumstances for ascertaining information about the physiology of the organ.

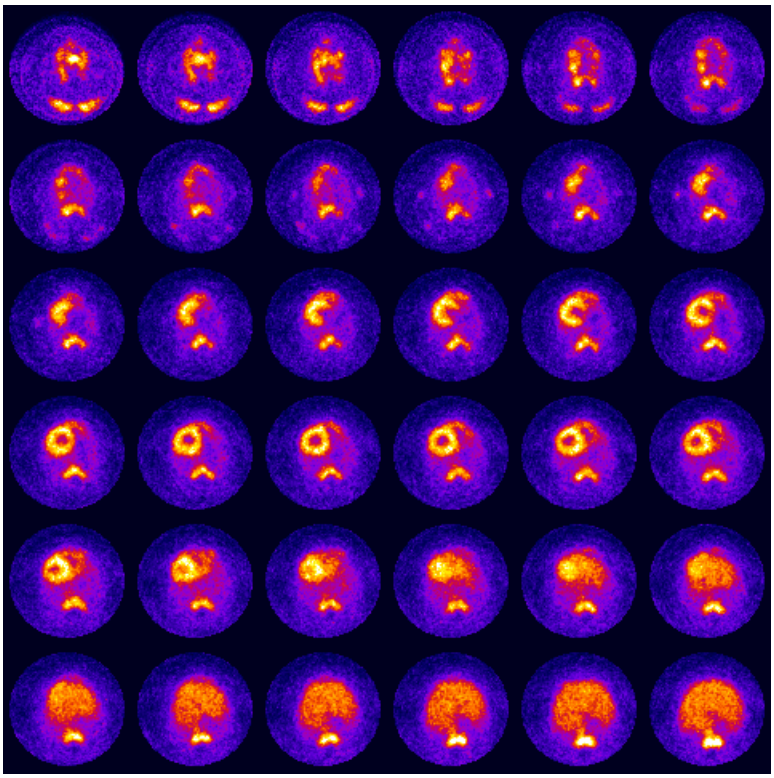

Figure 14. Summed static volume reconstructions (36 slices) from summed events over 66 rotations of data for a control WKY rat.

D. Sequence of Dynamic Reconstructions

Figure 15 shows a sequence of dynamic reconstructions of a transaxial slice through the heart of a control WKY rat at different time intervals. Each reconstruction represents a tomographic acquisition over 90 seconds. The washout of ^{123}I-MIBG within the heart region is evident in the late frames with the decreased intensity in the myocardium. The bottom right image is the reconstructed sum over 66 time frames. It is obvious from the first frame that the reconstruction represents the reconstruction of inconsistent projections corresponds to the time vary distribution of the radiopharmaceutical in the blood pool and the myocardium during the first rotation. The heart becomes more clearly visible in the third and fourth frames.

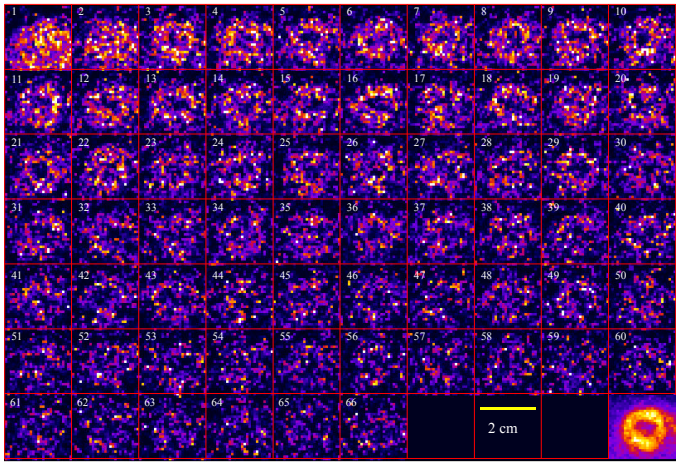

Figure 15. A dynamic sequence of reconstructions of a transaxial slice of a control WKY rat. The bottom right image is the reconstructed sum over 66 time frames.

E. Time activity curves in the blood pool and myocardium

Although not automatic, the ROI method is the standard method to obtain TACs within an organ. Figure 16 shows blood pool and myocardium TACs that were generated from ROI samples starting with the second rotation.

Figure 17 shows the 16 connected TACs in the blood pool. For each connected curve, the first 90-second part is from direct FA on projections. The enlarged view of the first 90-seconds is shown above each connected TAC. The rest of the curve is from the ROI method. Notice that in several cases there are double peaks for the curve during the first 90 seconds. It is anticipated that these represent interruption in the infusion with, in some cases, a final flush of the syringe containing still significant activity. It is felt that these curves do represent a true measure of the input function; however, more work needs to be done to verify this.

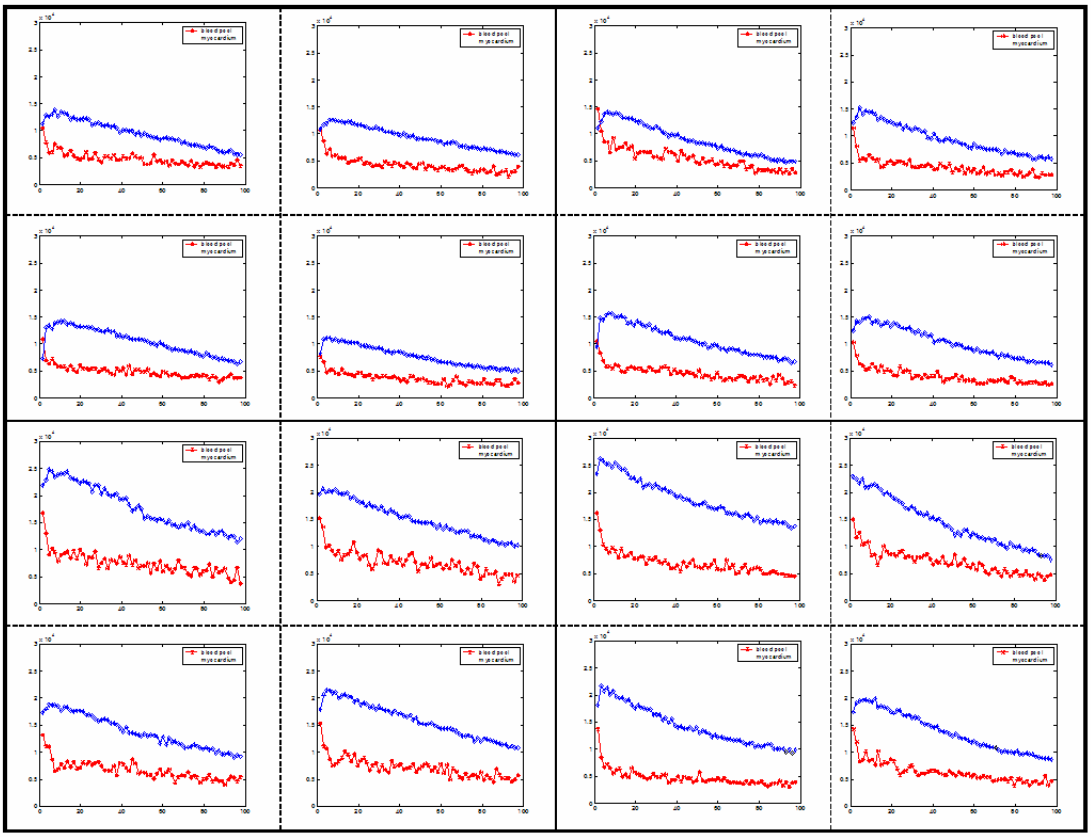

Figure 16. Blood and tissueTACs from the ROI method starting from the second rotation. Top left quadrant is for data collected on 03/02/2005. Top right quadrant is for 05/17/2005. Bottom left quadrant is for 08/16/2005; bottom right quadrant is for 11/29/2005. In each quadrant, thetop two figures are WKY (left) and SHR (right) for group 1; bottom two figures are WKY (left) and SHR (right) for group 2.

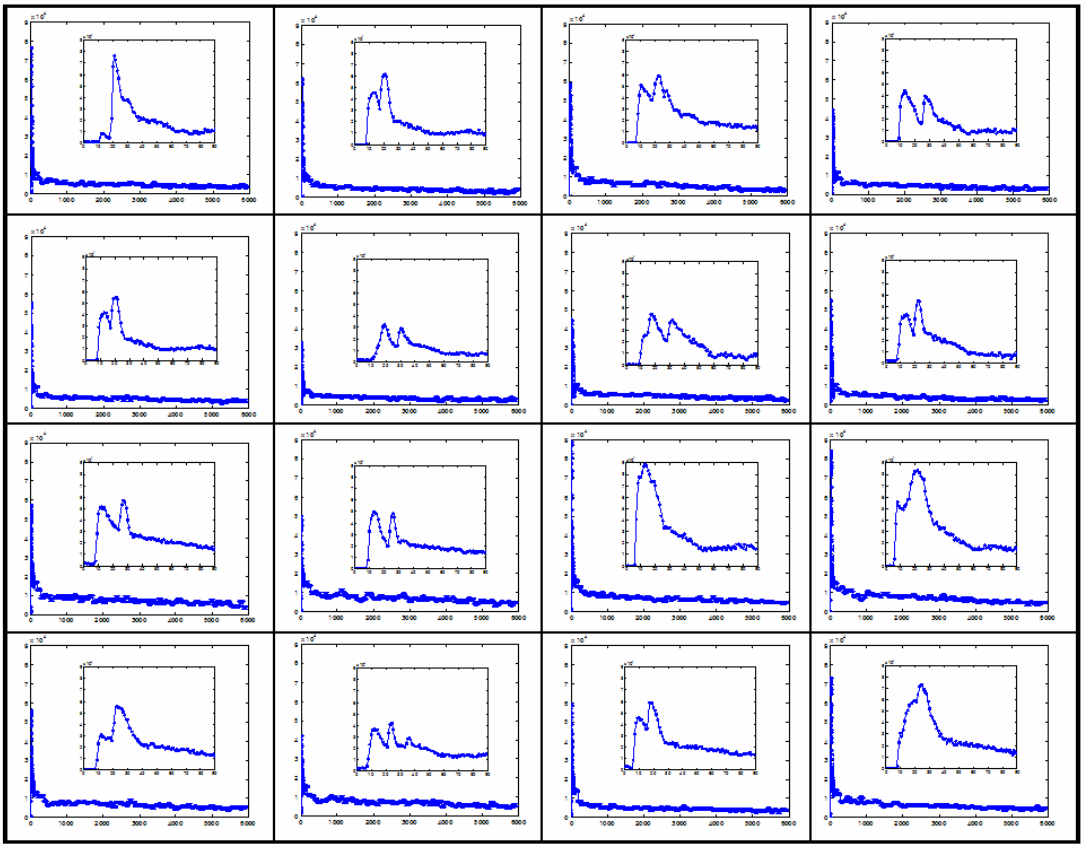

Figure 17. TheTACs corresponding to the blood input function for compartment analysis. In each plot, two curves are presented. The curve presented in the smaller figure corresponds to the first 90 seconds of the acquisition calculated by applying FA directly to the projections, and is an enlargement of the beginning of the main curve. Top left quadrant is for data collected on 03/02/2005; top right quadrant is for 05/17/2005; bottom left quadrant is for 08/16/2005; bottom right quadrant is for 11/29/2005. In each quadrant, top two figures are WKY (left) and SHR (right) for group 1; bottom two figures are WKY (left) and SHR (right) for group 2.

G. Compartmental Modeling

We applied the non-linear least squares fit method using both blood pool and myocardium TACs to 16 animal studies and obtained estimates of the washin and washout rate of ^{123}I-MIBG in the myocardium. Figure 18 shows the fit for the myocardium TACs. The ROI measurements provided the values of the myocardial curve for each point, except the first one for which the FA was performed directly on the projections. We approximate the value of the first point (first point on the blue curve, Fig. 18) as the average of zero and the value of the second point.

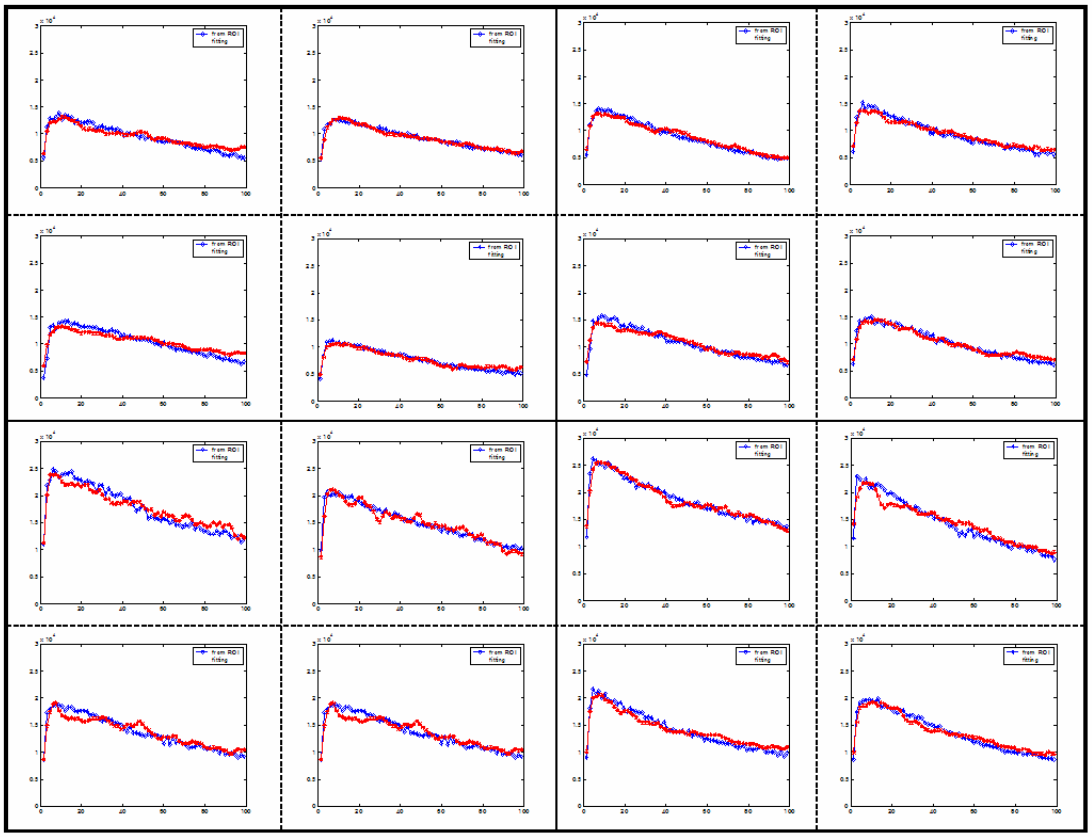

Figure 18. Results of two compartment model fitting. The blue curve corresponds to the ROI measurement and the red curve corresponds to the fit. Top left quadrant is for data collected on 03/02/2005; top right quadrant is for 05/17/2005; bottom left quadrant is for 08/16/2005; bottom right quadrant is for 11/29/2005. In each quadrant, top two figures are WKY (left) and SHR (right) for group 1; bottom two figures are WKY (left) and SHR (right) for group 2.

Figure 19 shows the washout parameters for the myocardial tissue over time. The error bars represent one standard deviation. Notice that the washout rates were fairly similar during the first three studies. Remember that these studies were performed during the second year of life for all of the rats. In the third study, it appears that the SHRs begin to demonstrate a faster washout than that of the normal tensive WKY rats. In the final study the SHR from Group 1 definitely shows a higher washout than the other rats. This SHR died a month later. However, admittedly, the other SHR did not have a significantly higher washout than that of the control rats. The faster washout corresponds to what is expected with a compromised heart (Henderson 1988, Arimoto 2004). Table 4 tabulates the washin (K_{21}) and washout (K_{12}) parameters for the series of studies.

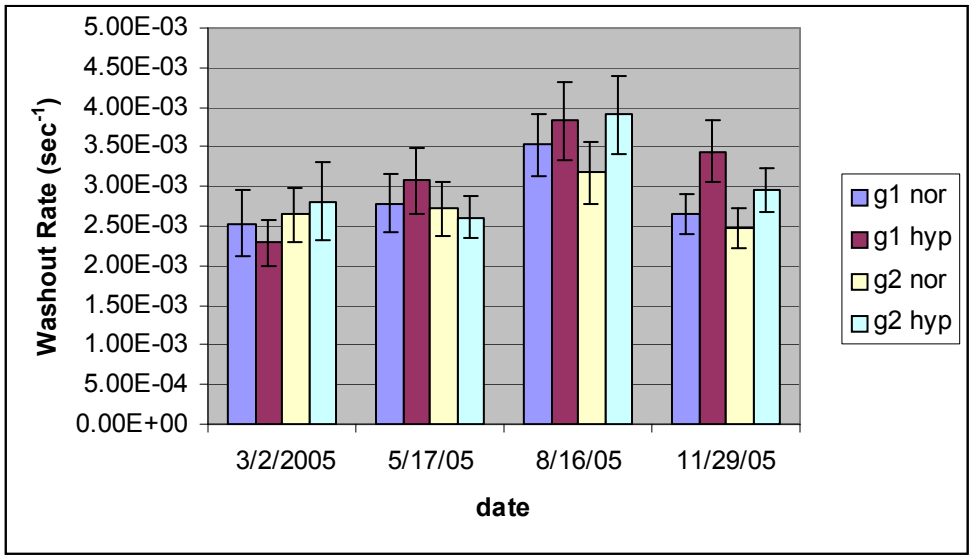

Figure 19. Washout rates for the four groups of experiments. The error bars are one standard deviation.

			03/02/2005	05/17/2005	08/16/2005	11/29/2005
g1 nor	Washin (sec^{-1})	Mean	5.76E-03	4.42E-03	8.33E-03	7.15E-03
		Dev	7.54E-04	5.42E-04	8.78E-04	6.37E-04
	Washout (sec^{-1})	Mean	2.54E-03	2.78E-03	3.52E-03	2.64E-03
		Dev	4.13E-04	3.62E-04	3.97E-04	2.53E-04
g1 hyp	Washin (sec^{-1})	Mean	5.04E-03	6.88E-03	8.12E-03	6.74E-03
		Dev	5.97E-04	8.77E-04	9.67E-04	7.24E-04
	Washout (sec^{-1})	Mean	2.29E-03	3.07E-03	3.83E-03	3.44E-03
		Dev	2.93E-04	4.18E-04	4.84E-04	3.92E-04
g2 nor	Washin (sec^{-1})	Mean	5.65E-03	6.30E-03	6.55E-03	7.41E-03
		Dev	6.95E-04	7.39E-04	7.51E-04	7.21E-04
	Washout (sec^{-1})	Mean	2.64E-03	2.72E-03	3.17E-03	2.48E-03
		Dev	3.51E-04	3.43E-04	3.90E-04	2.60E-04
g2 hyp	Washin (sec^{-1})	Mean	6.61E-03	5.86E-03	8.73E-03	5.52E-03
		Dev	9.85E-04	6.44E-04	1.04E-03	5.55E-04
	Washout (sec^{-1})	Mean	2.81E-03	2.61E-03	3.91E-03	2.96E-03
		Dev	4.95E-04	2.74E-04	4.95E-04	2.78E-04

Table 4. Fitted compartment model parameters with errors. K_{21} is the washin and K_{12} is the washout rate constant for the two-compartment model in Fig. 9.

In the last group of studies (Fig. 19), it is noticed that the washout for the hypertensive SHR are higher than the normotensive WKY. The g1 hyp died one month later (see Table 2). To get a measure of the pharmokinetics of both the flow times extraction (K_{21}) washin and the washout, the distributions volumes were calculated. The results are shown in Fig. 20 for the series of studies. Notice that the distribution volumes for the hypertensive rats were much less than the WKY controls. However, the SHR that died had a somewhat better distribution volume than that of the other SHR. Also, it is somewhat puzzling that the distribution volumes for the WKY controls are significantly higher than their distribution volumes in the previous study on 8/16/05. Is this a real effect or a problem of non uniqueness? The results in Fig. 20 need to be verified by computer simulations.

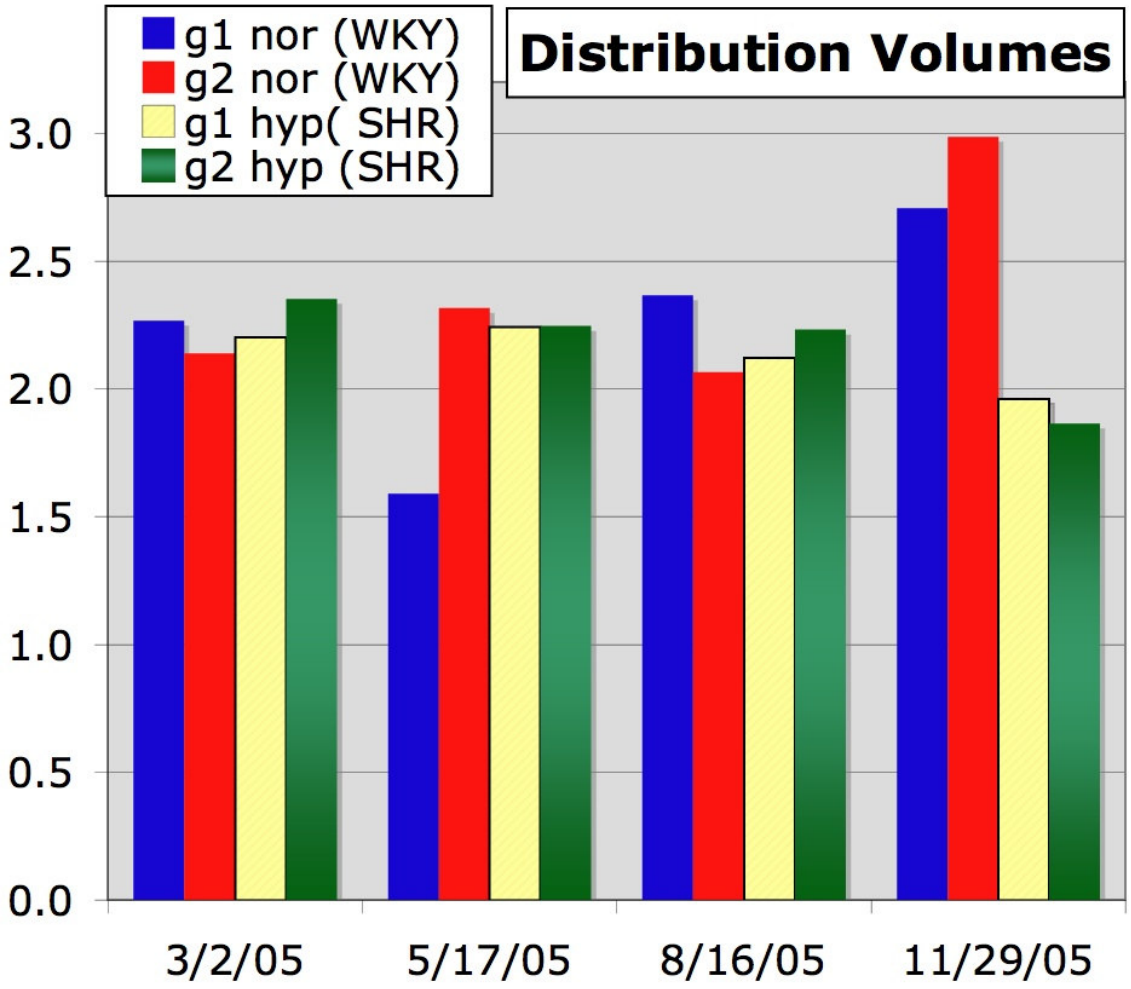

Figure 20. Distribution volumes for the four groups of experiments. The distribution volumes were determined as the ratio of K_{21}/K_{12} using the values in Table 4.

There is significant changes in collagen as shown in Fig. 21. These rats survive approximately 2 years. At death or when sacrificed, the heart is removed and weighed. The examination of the hearts demonstrate that the SHR have larger hearts due to hypertrophy (see Table 2) and the lungs were filled with fluid indicative of congestive heart failure. Also, results of staining (Fig. 21) show significantly more collagen content in the SHR hypertrophic heart. Trichrome staining of the mid left ventricle section of one SHR (died of HF) and one WKY control shows significant increase in collagen content (blue) in the LV wall of the SHR [Figure 21(lower right)] compared with the WKY rat [Figure 21(lower left)]. Also, the SHR showed more stainning for sympathetic innervation of the endocardium than the WKY control.

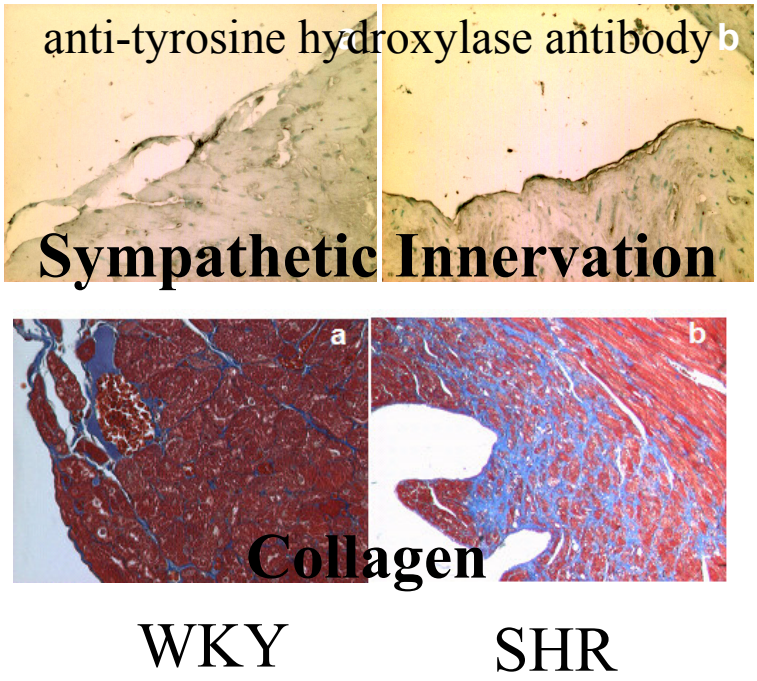

Figure 21. Comparison of immunohistochemical staining in SHR and WKY rat cardiac tissue samples. Trichrome stain shows less blue in (lower left) WKY rat than (lower right) SHR tissue sample. The SHR had a collagen volume fraction of 33.41% compared with 11.86% for the WKY rat. Staining with anti-tyrosine hydroxylase antibody shows that the (upper left) WKY rat has less endocardial sympathetic nerve density than the (upper right) SHR.

IV. DISCUSSION AND CONCLUSION

In this work, a calibration and reconstruction procedure for the dual head pinhole SPECT system used in our laboratory was presented. In the calibration, we modeled the angle variant effects caused by the gravitational torque of the transaxial and axial mechanical shifts. The geometrical parameters for both pinholes were obtained by a non-linear least square fitting method. An iterative image reconstruction method, which properly accounted for the point spread function using a multi-ray technique, was developed.

Using the developed methodology, a dynamic ^{123}I-MIBG pinhole SPECT imaging protocol was used to assess the distribution of the sympathetic innervation and function in normal WKY rats and SHRs. The proposed protocol was designed to require less time than a traditional ^{123}I-MIBG imaging protocol for the evaluation of sympathetic nervous system function. It has the potential to more accurately measure the kinetic parameters of MIBG uptake since the tomographic information is included. The FA method was applied directly to tomographic projection data corresponding to the first rotation of the camera in order to obtain the input function during the first 90 seconds. This was done because of the 6 to 8 seconds recirculation time in a rat, resulting in a fast passage of the tracer through the blood and exchange with lung, heart, and other organs causing the projections to be inconsistent during the first 90 seconds of the acquisition. Starting from the second rotation, the projections became relatively consistent, and a standard tomographic reconstruction was used for tomographic acquisitions of rotations 2 through 66. ROI measurements applied to the reconstructed images were used to obtain the TACs for the blood pool and the myocardium. The FA method was applied to the dynamic sequence of reconstructions (Sitek 2000); however, we found that the TAC corresponding to the myocardium extracted by FA agreed well with the ROI method. Thus the ROI measurements were used for the TACs after the first rotation of the camera detectors.

After TACs were obtained for both blood pool and myocardium, compartment modeling was used to obtain the washin and washout kinetic parameters for a two-compartment model. The results suggest that towards the end of a rats' life, the ^{123}I-MIBG washout rate is higher in hypertensive rats than it is in the normal rats, whereas during earlier life there is virtually no difference in ^{123}I-MIBG washout between hypertensive and normal rats. However, we emphasize that the results are not statistically significant, since experiments were performed on only 4 rats (2 WKY and 2 SHR).

There are several limitations of the current study that we would like to point out. One shortcoming is the determination of connecting TACs by using the fact that the value of the end

point from the direct FA method should be equal to the first point from the reconstructed images. Because of noise in the data, this procedure may be inaccurate. Another shortcoming is the problem of non-uniqueness. One solution is to address the non-uniqueness during the optimization using an orthogonal constraint, as presented in Sitek *et al.* (2002). This however would increase the numerical complexity considerably. We showed (Sitek 2001) that in order to derive a more accurate estimation of factors from projections, more detectors in the acquisition need to be used. In the current setting, we used two detectors positioned 180° apart, which resulted in duplication of data. In the future we plan to use 2 detectors positioned with a relative angle of 90°, which should result in better performance of the FA method applied to projection data (Sitek 2001). We will also consider investigating other methods applicable to reconstruction of inconsistent data, such as dSPECT (Farncombe 2002).

Another important issue that needs to be addressed is collimator penetration when imaging with ^{123}I. The pinhole collimator (Fig. 1) that we used in this study was designed to stop photons with energies up to 140 keV. An experiment was performed to evaluate the amount of penetration through the pinhole collimators of higher energy emissions from ^{123}I. The detector heads with pinhole collimators (1.5 mm apertures) were positioned 180˚ apart, separated by 10 cm. A 4 mCi source of ^{123}I in a 50-ml syringe was positioned between the pinhole collimators in a manner similar to how the rat was positioned. The energy spectrum was measured using camera Pulse Height Analysis (PHA) [Fig. 22(a)]. First, the counts acquired in the ^{123}I 20% energy window were measured. Next the pinholes were covered with 1 cm thick lead bars and the energy spectrum [Fig 22(b)] and counts were measured again. This yielded 18% penetration for Head 1 and 26% penetration for Head 2. The difference was due to the fact that the source was placed 1.8 cm off center, yielding the same background in both detectors but an increased primary for Head 1, which was closer to the source. This background was summed over the entire field of view, whereas the heart covers a much smaller portion of that field of view. Even still, this background will bias our kinetic data but it is sufficiently low enough to not significantly affect the values.

Figure 22 shows some interesting features in the energy spectra for ^{123}I obtained from the SPECT system. Notice the 159 keV peak in Fig. 22(a). The lower energy peak is the 27 keV emissions, followed on the right by an increasing small Compton edge of 61 keV, then followed by lead x-rays at 80-90 keV, and then a backscatter peak around 98 keV. There are also higher energy emissions (248, 281, 347 keV) around 300 keV, including the summation of two 159 keV photons equal to 318 keV, and emissions (440, 506, 529, 538,625, 688 keV) that straddle 500 keV. The highest emissions are at 736 keV and 784 keV. Figure 23 shows the spectrum taken

from a well counter for a sample on a different day, which shows some emissions around 500 keV and some around 750 keV.

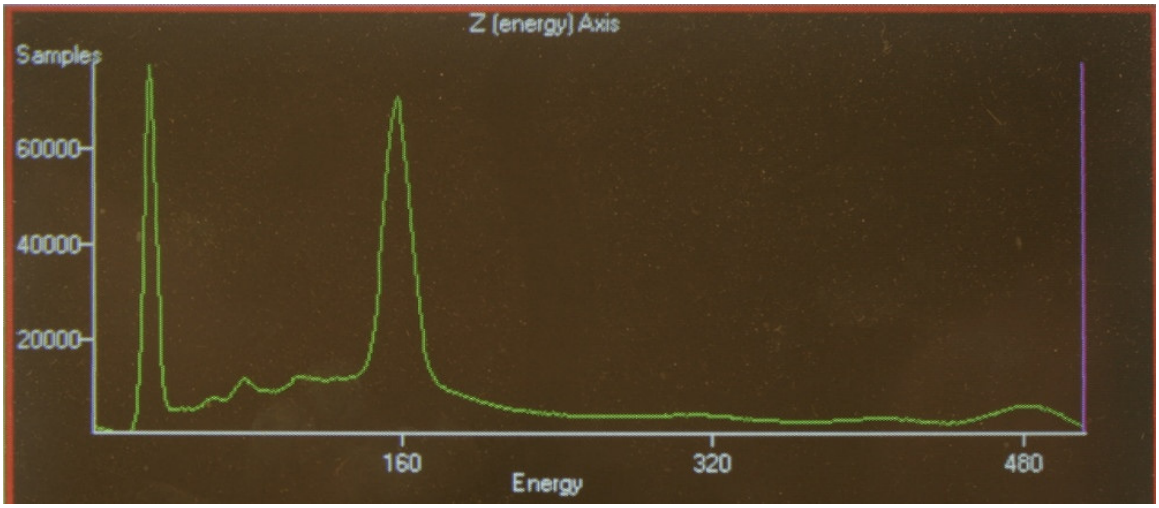

(a)

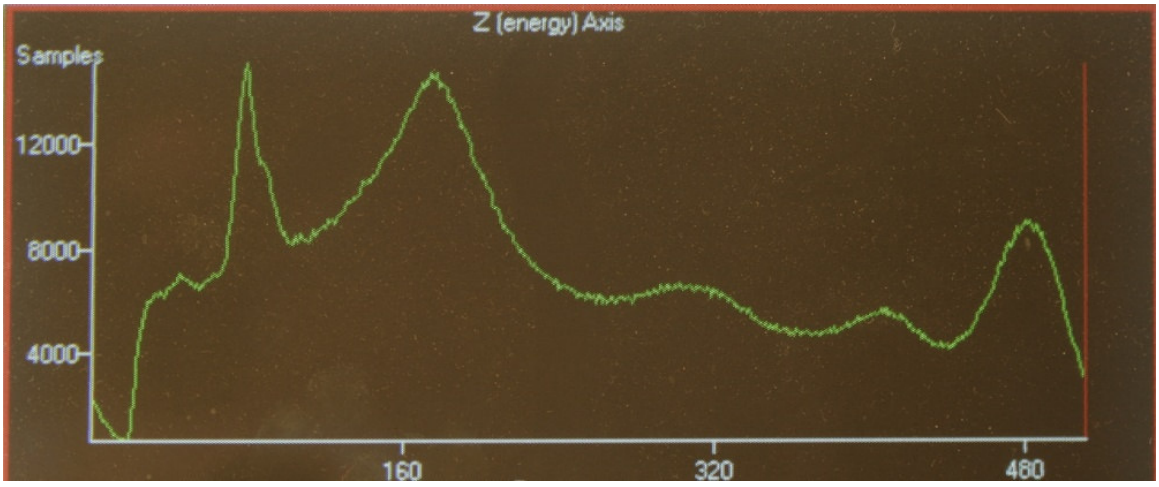

(b)

Figure 22. Energy spectrum for ^{123}I obtained from pinhole SPECT system (Fig. 1). (a) Spectrum with the source placed 25 cm from the 1.5 mm pinhole aperture. (b) Spectrum with the source placed 25 cm from the 1.5 mm pinhole aperture, which was plugged with lead. The lower peak of lead x-rays are now more pronounced.

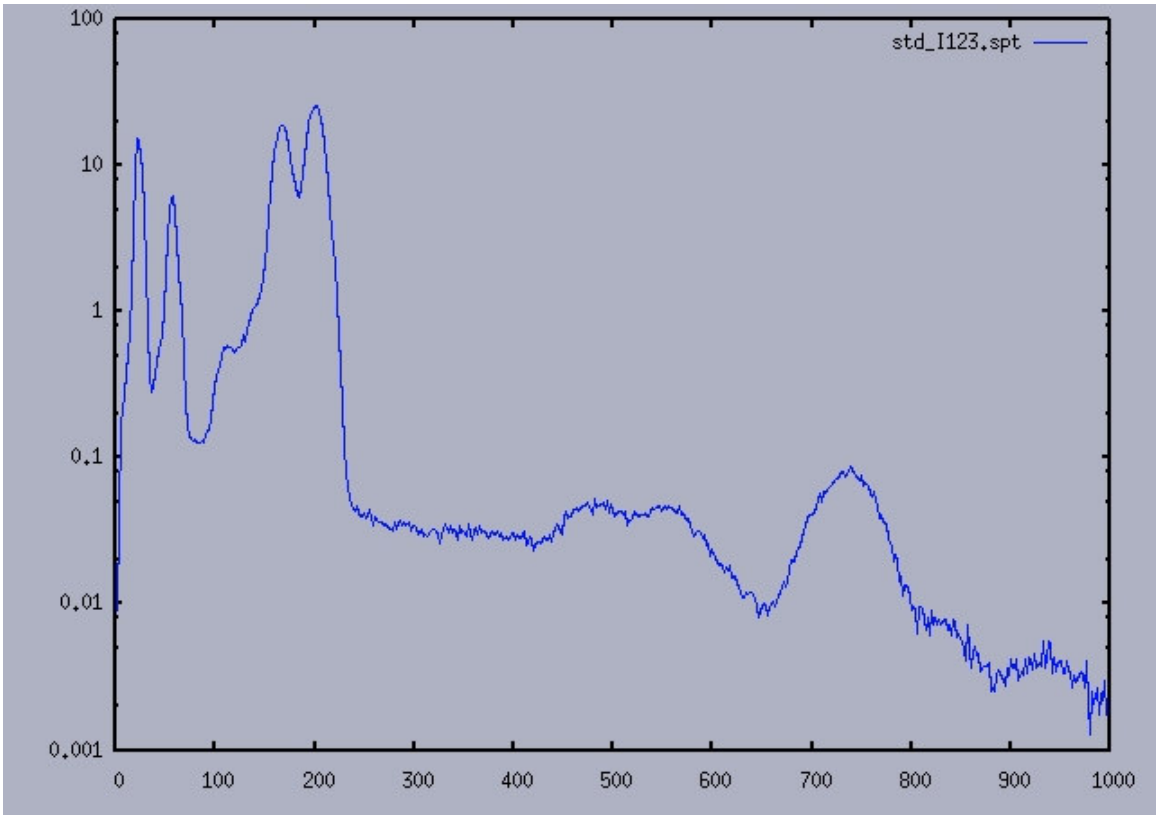

Figure 23. Energy spectrum for ^{123}I obtained from well counter. The spectrum shows disintegrations beyond the maximum energy of 512 keV obtained with the SPECT system. The additional peaks around 54 keV and 186 keV are the summation of two 27 keV emissions and the sum of a 27 keV emission and a 159 keV emission, respectively.

The cardiac autonomic nervous system consists of both sympathetic and parasympathetic innervation (Bengel 2004). Each system differs in their major neurotransmitters. The primary sympathetic transmitter is norepinephrine and the primary parasympathetic transmitter is acetylcholine; each exhibit stimulating or inhibitory effects in target tissues via adrenergic and muscarinic receptors. Sympathetic nerves extend from the base toward the apex of the left ventricle and penetrate the myocardium from the epicardial surface to the endocardial surface alongside the coronary vessels. (Patel 2002) The sympathetic neuron density appears to be lower in the endocardial layer than in the epicardial layer; or some functional difference might exist between the layers and is reflected in differences in ^{125}I-MIBG imaging (Matsunari 1993). Norepinephrine is synthesized within the neurons. First, DOPA is synthesized from tyrosine, which is subsequently converted to dopamine by DOPA decarboxylase. Dopamine is transported (requiring energy) into storage vesicles where norepinephrine is synthesized from dopamine

through the enzyme dopamine β-hydroxylase**.** Neuronal stimulation leads to norepinephrine release through exocytosis. Release is regulated by a number of presynaptic receptor systems. One system involves α_2-adrenergic receptors, which provide negative feedback for exocytosis. Most of the norepinephrine released from the presynaptic neuron undergoes reuptake by the energy dependent uptake-1 mechanism and recycles into vesicles or is metabolized in the cytosol, and only a small amount of released norepinephrine actually activates postsynaptic receptors on the surface of the myocyte. The non energy-dependent uptake-2 system will remove norepinephrine from the synaptic cleft into the myocyte as well as other nonneuronal tissue, and dominates at higher concentrations of norepinephrine and is probably the result of passive diffusion. The postsynaptic receptors are membrane-bound proteins, which are classified in subtypes according to their biochemistry characteristics. β-Adrenoceptors [β_1- (80%) and β_2-subtypes (20%] (Carrio 2001) exert chronotropic (increased heart rate), dromotroipic (enhanced atrioventricular conduction), and inotropic (augmented contractility) effects. α-Adrenoceptors (α_1- and α_2-receptors) account for about 15% of cardiac adrenergic receptors and α_2-receptors are both present postsynaptically and presynaptically. Norepinephrine binds to β_1-receptors, whereas epinephrine binds to β_2-receptors. β_1-receptors are located mainly in the synaptic cleft, whereas β_2-receptors are located far from the synaptic cleft for easier access for the hormone epinephrine. The β-adrenoceptors are coupled to G protein subunits and stimulation by either norepinephrine or epinephrine increases adenylyl cyclase activity. This subsequently leads to intracellular cyclic adenosine monophosphate (cAMP) formation and phosphorylation of intracellular proteins, mediated by protein kinases, and influencing calcium transients and repolarization. When prolonged excessive stimulation of adrenergic receptors takes place, the first consequence is desensitization of adrenoceptors, followed by down regulation with enhanced receptor degradation and decreased receptor synthesis. The next step is downregulation of adenylyl cyclase resulting in a clinical consequence of decreased myocardial reserve and impaired exercise capacity.

^{123}I-MIBG is used to asses the innervation of the sympathetic nervous system in the heart and is thought to share the same uptake, storage, and release mechanisms as norepinephrine (NE) in the nerve terminals but it is not metabolized (Wieland 1981b, Nakajo 1986). Two mechanisms are known for the presynaptic uptake of MIBG. One, is a neuronal energy-dependent uptake-1 mechanism (DeGrado 1995, Nakajo 1986, Glowniak 1993, Guilloteau, Pissarek 2002). The second, is a nonneuronal energy independent uptake-2 mechanism (DeGrado 1995, Pissarek,

2002). This nonneuronal uptake-2 mechanism dominates at higher concentrations and probably results from passive diffusion. Neuronal uptake is predominantly determined by the uptake-1 mechanism because when imaging, only an extremely small quantity of ^{123}I-MIBG is usually injected (Carrio 2001). Clinically, ^{123}I-MIBG is used in the diagnosis of heart failure (congestive heart failure, dilated cardiomyopathy, hypertrophic cardiomyopathy), evaluation of neuronal function after heart transplant, evaluation of heart function with diabetes and during chemotherapy, and in the evaluation of arrhythmias. A high washout rate means increased adrenergic activity (Patel 2002). SHRs seem to develop similarities to patients with heart failure. They develop a generally enhanced sympathetic tone and a downregulation of cardiac β_1-receptors (Dubois 1996, Bohlender 2000, Pissarek, 2002). In our work a 2-compartment model was used to model the kinetics of ^{123}I-MIBG. The data seemed to fit this model well but more work is needed to verify if this is the best model to represent the physiology of MIBG. The role of alterations of the supracardiac receptor population for cardiac norepinephrine turnover, the density or activity of uptake-1 transporters, and the perfusion of cardiac microcompartments have not been clarified; and thus, their influence remains open (Pissarek 2002).

In future work we will address the limitations cited above. We also propose to perform a repeat study where we compare results using ^{123}I-MIBG with results using selected neurotransmitters and analogs that can be tagged with positron emitters (Bengel 2004). Pissaek *et al.* (2002) have previously shown better results with ^{18}F-fluorometaraminol than with ^{123}I-MIBG. It would also be interesting to use molecular imaging to investigate the effect of exercise on those with heart failure (Sato 2003). Cardiac ^{123}I-MIBG uptake of the delayed image can predict the degree of increase in adrenergic drive to the heart during sympathetic stimuli induced by exercise in patients with chronic heart failure (to measure reduced exercise activity). Also, ^{123}I-MIBG imaging has shown that renal transplantation provides improvement in uremic cardiac sympathetic neuropathy (Kurata 2004). This research illustrates the important interplay between renal and cardiac function.

APPENDIX

A. Introduction

The results presented in this report were due to the development and implementation of algorithms by the first author (Jicun Hu) . After he left LBNL for a position at Siemens Medical Systems in Knoxville, TN, the second author (Rostyslav Boutchko) continued to develop algorithms for reconstructing the dynamic pinhole SPECT data from slow camera rotation. This involved developing computer code both for the calibration of the geometry and the modeling of the pinhole projections used by the reconstruction algorithm. These developments are presented in this Appendix.

B. Calibration of the Dual Head Pinhole System

In order to overcome effect of geometric misalignment, we automated and improved the calibration routine presented in subsection **II.*B***.

The first stage of the calibration involves determining coordinates (u,v) of the calibration point source projections onto the detector plane. For each detector head h and gantry rotation angle θ, the detected signal S is represented as a combination of I Gaussians, where I is the number of the radioactive point sources in the calibration object.

$$S_\theta^h(u,v) = \sum_{i=1}^{I} A_{i\theta} \exp\left[-\left((u-u_{i\theta})^2 + (v-v_{i\theta})^2\right)/B_{i\theta}^2\right].$$

Using a Matlab®-based optimization algorithms, measured trajectories $\left(u_{\theta,i}^{\text{img}}, v_{\theta,i}^{\text{img}}\right)$ for three of the points were calculated as shown in Figure A1. Continuity of the trajectories as well as continuity of $A_{i\theta}$ and $B_{i\theta}$ are used as additional constraints.

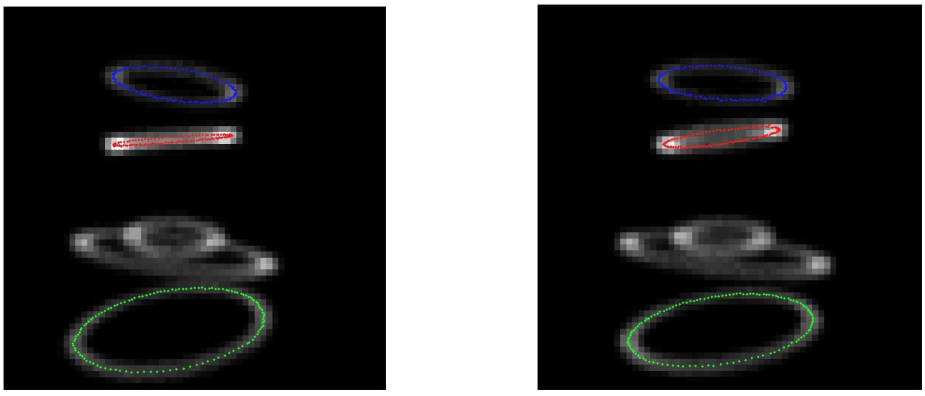

Figure A1. Summed projections of the calibration phantom scan for two detector heads. Color markers show positions of centers of the Gaussian fits to the traces of three of the point sources used for the calibration.

Once three measured trajectories are known for both detectors, we use parametric modeling to fit the instantaneous positions of the detectors as well as the spatial positions of the point sources.

- θ: Angle of gantry rotation about z-axis.

1. ${}^{h}d$: Distance from the pinhole to the axis of rotation.
2. ${}^{h}f$: Distance from the pinhole to the detector plane.
3. ${}^{h}\varphi$: Twist angle, rotation of the detector plane about the tangential u axis.
4. ${}^{h}\psi$: Tilt angle, rotation about the radial axis (coinciding with y axis for q = 0).

5-7. ${}^{h}m_t(\theta) = {}^{h}m_{t,0} + {}^{h}m_{t,s} \sin\theta + {}^{h}m_{t,c} \cos\theta$: Transaxial shift (along u-axis).

8-10. ${}^{h}m_a(\theta) = {}^{h}m_{a,0} + {}^{h}m_{a,s} \sin\theta + {}^{h}m_{a,c} \cos\theta$: Axial shift (along z-axis).

11. ${}^{h}e_u$: Electronic shift in u-direction: shift between the true geometric center of the detector plane and electronically-measured u=0.
12. ${}^{h}e_v$: Electronic shift in v-direction.

All of these parameters except for the twist angle are displayed in Figure A2

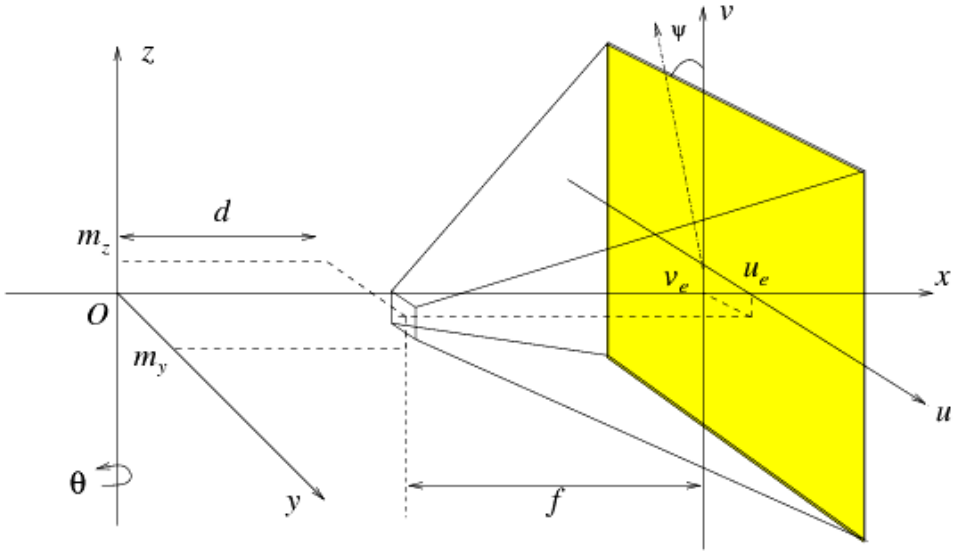

Figure A2. Illustration of dual head pinhole SPECT system and geometrical parameters. Only one detector head is shown in the figure.

The total number of geometric parameters for each head is twelve. However, one of the parameters, the mean axial shift (${}^{h}m_{a,0}$) has to be taken into account only as a difference of axial shifts between the two heads. We take it into account by imposing a constraint

$$ {}^{1}m_{a,0} = {}^{2}m_{a,0} , $$

thus reducing the total number of free geometric parameters to 23.

It is important to specify a consistent order of introducing the described geometric

corrections to the system. Below, we illustrate the transformations that produce the true coordinates of a detector cell (*u, v*) $\mathbf{r}_d$ and of the pinhole center $\mathbf{r}_p$ for gantry rotation angle $\theta = 0$. Before the corrections, these coordinates are

$$\begin{aligned} \mathbf{r}_{d0} &= (d + f, u, v), \\ \mathbf{r}_{p0} &= (d \quad\;\; , 0, 0). \end{aligned} \tag{A1}$$

First, we shift the detector cell coordinates by the electronic shift:

$$\mathbf{r}_{d1} \;=\; \mathbf{r}_{d0} + (0,\, e_u,\, e_v) = (d + f,\, u + e_u,\, v + e_v).$$

Second, we apply rotation by the tilt angle, followed by the rotation by the twist angle, with the center of the rotation being the exact center of the detector in the unperturbed case:

$$\begin{aligned} \mathbf{r}_{d2} &= (d + f,\; 0,\; 0) \;+\; R_{\varphi\psi}\,(0,\, u + e_u,\, v + e_v), \\ \mathbf{r}_{p2} &= (d + f,\; 0,\; 0) \;+\; R_{\varphi\psi}\,(-f,\; 0,\; 0), \end{aligned}$$

where

$$R_{\varphi\psi} \;=\; \begin{pmatrix} 1 & 0 & 0 \\ 0 & \cos\varphi & -\sin\varphi \\ 0 & \sin\varphi & \cos\varphi \end{pmatrix} \begin{pmatrix} \cos\psi & 0 & -\sin\psi \\ 0 & 1 & 0 \\ \sin\psi & 0 & \cos\psi \end{pmatrix}. \tag{A2}$$

Then, we apply the mechanical shifts along *y* and *z* axes:

$$\begin{aligned} \mathbf{r}_{d3} &\;=\; \mathbf{r}_{d2} + (0,\, m_t,\, m_a), \\ \mathbf{r}_{p3} &\;=\; \mathbf{r}_{p2} + (0,\, m_t,\, m_a). \end{aligned}$$

Finally, we apply the gantry rotation as multiplication by the rotation matrix R_θ

$$R_\theta \;=\; \begin{pmatrix} \cos\theta & \sin\theta & 0 \\ -\sin\theta & \cos\theta & 0 \\ 0 & 0 & 1 \end{pmatrix} \tag{A3}$$

The final expressions for $\mathbf{r}_d$ and $\mathbf{r}_p$ are

$$\begin{aligned} \mathbf{r}_d &\;=\; R_\theta \left[(d + f,\, m_y,\, m_z) \;+\; R_{\varphi\psi}\,(0,\, u + e_u,\, v + e_v) \right], \\ \mathbf{r}_p &\;=\; R_\theta \left[(d + f,\, m_y,\, m_z) \;+\; R_{\varphi\psi}\,(-f,\, 0,\, 0) \right], \end{aligned} \tag{A4}$$

where we delete the gantry head index *h* for the sake of convenience.

For any point source at position $\mathrm{r_s}$, equations (A4) can be used to compute the estimated projection coordinates of this point onto the detector *h*: $(u^{est}_{i,\theta,h}, v^{est}_{i,\theta,h})$. We use three point sources out of five in the calibration phantom in Figure 5 in order to obtain the 23 geometric parameters for the two-head system. The parameters are obtained by non-linear minimization of the following chi-square functional:

$$\chi^2 \;=\; \sum_h \sum_i \sum_\theta \left\{ \left[{}^h u^{\mathrm{est}}_{\theta,i} - {}^h u^{\mathrm{img}}_{\theta,i} \right]^2 - \left[{}^h v^{\mathrm{est}}_{\theta,i} - {}^h v^{\mathrm{img}}_{\theta,i} \right]^2 \right\}, \tag{A5}$$

where h is the index of the detector heads, i is the index for the points in the object space, θ is the index of the view angle, $(u_{i,\theta,h}^{img}, v_{i,\theta,h}^{img})$ is the coordinate of the measured centroid of the projection of the point source. The resulting fits are shown in Figure A3.

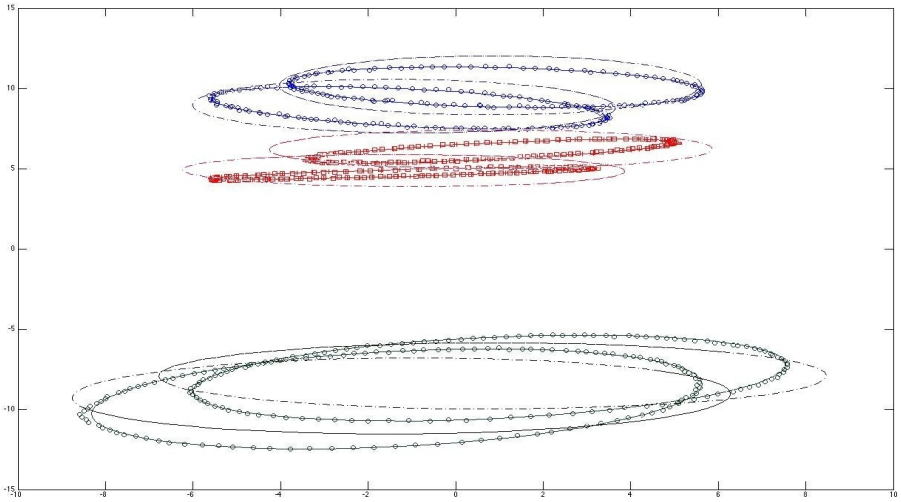

Figure A3. Twelve-parameter fits to the detected trajectories of the point sources whose segmentation is illustrated in Figure A1. Dashed gray lines show 8-parameter (gantry-angle-independent) fits of the same trajectories.

C. Reconstruction of Data Acquired with the Dual Head Pinhole System

In this subsection, we provide a more detailed derivation of equation (13) which is used to construct the system matrix used in the image reconstruction from projections.

Assume there is a unit of activity within voxel j. The voxel is at distance $d + f$ from the detector, where f is pinhole-detector distance. Consider the projection of the detector onto area element dA of detector pixel i through the element ds of the pinhole, as shown in Figure A4. First, we need to determine the projections of these area elements onto the plane perpendicular to the ray propagation direction:

$$ds_p = ds \cos \alpha = ds \sin \theta,$$
$$dA_p = dA \sin \theta.$$

Element dA will detect signal from the fraction dV_j of the voxel:

$$dV_j = l_{ij}\, dA_p\, d^2 / f^2, \tag{A7}$$

where l_{ij} denotes the path of the propagation ray defined by indices i and j through the voxel j. Pinhole sensitivity, or the fraction of the total radiation from dV_j as seen at the pinhole area element is equal to the fraction of solid angle created by ds_p in a sphere of radius $d / \cos \theta$, or

$ds_p \cos\theta / 4\pi d^2$. Combining this with (7) and integrating over both pixel area and the pinhole area, we obtain the final expression for the system matrix entry *ij*:

$$\alpha_{ij} = \frac{A\, s \left\langle l_{ij} \right\rangle}{4\pi f^2} \sin^4 \theta, \qquad \text{(A8)}$$

where $\left\langle l_{ij} \right\rangle$ denotes the average value of the path length of the propagation ray through voxel *j*.

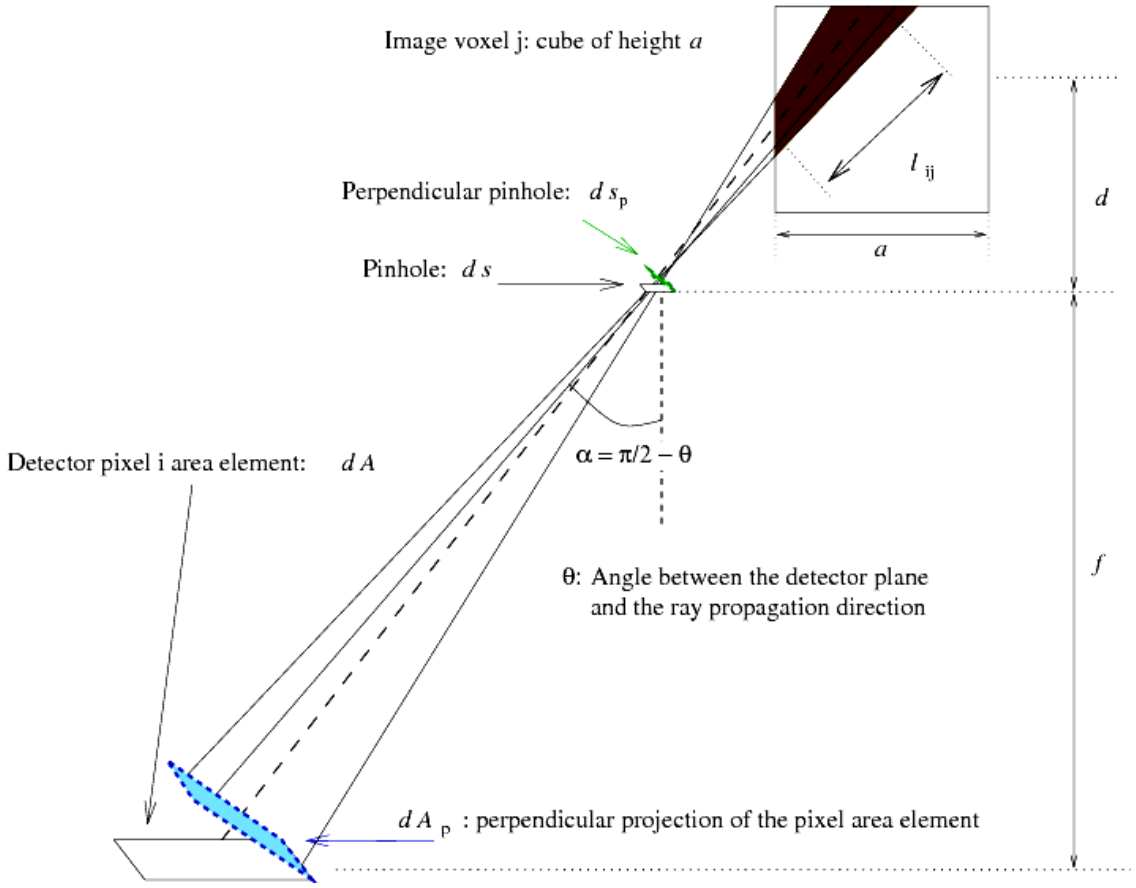

Figure A4. Pinhole geometry: explanation of the sensitivity expression (A8), which is used to compute the system matrix.

The approach presented corresponds to the so-called ray-driven forward- and backprojection realization. Within ray-driven methodology, the geometric blurring due to finite size of the pinhole and finite size of the detector pixels is implemented by tracing multiple rays as described in Section **II.*C***. In the future, we consider adding attenuation correction functionality by multiplying sensitivity (A8) by the attenuation factor that can be computed if X-ray CT images of the scanned animal are available. Also, we are studying the possibility of translating to a voxel-based projection scheme which would

allow us to add experimentally measured blurring kernels to correct for effect of penetration and scatter.

D. Results

In Figure A5, we show the reconstruction of a rat study using the fatty acid ^{123}I-BMIPP. The rat was a WKY rat. System geometry calibration was done using the above-described approach. Figure (A1) and (A3) show two intermediate steps of the calibration procedure for this scan.

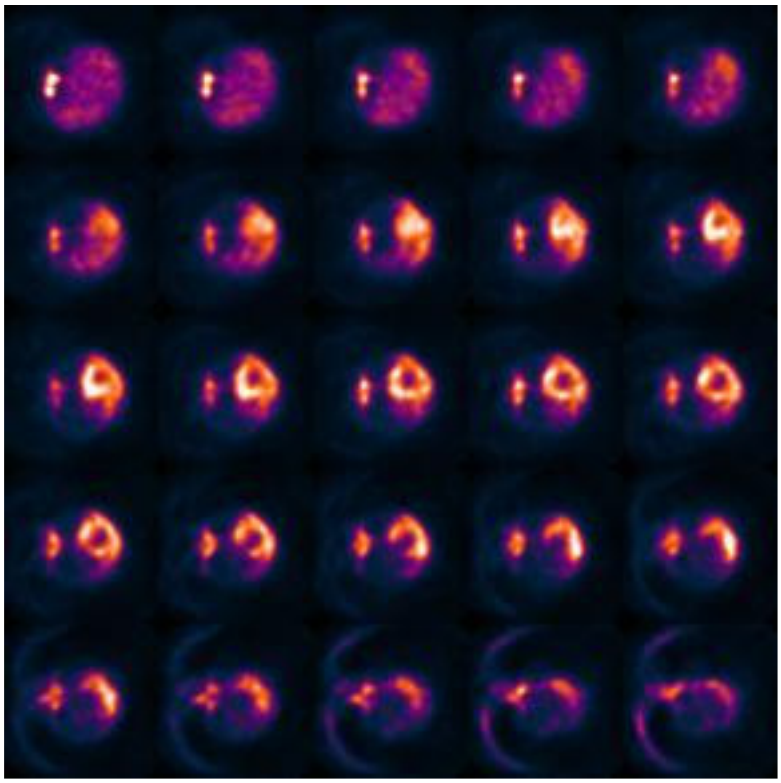

Figure A5. Reconstructed transaxial slices in of the heart region. The voxel size was 0.85 mm.

ACKNOWLEDGEMENTS

We would like to thank Kathleen Brennan, D.V.M. for assistance with the rat experiments, Stephen Hanrahan for preparing the ^{123}I-MIBG studies, and John Huberty, M.Sc. at UCSF for supplying the MIBG precursor. We also want to thank Benjamin M. W. Tsui, Ph.D. and Yuchuan Wang, Ph.D. at Johns Hopkins University for supplying the point source calibration phantom.

REFERENCES

Acton PD, Hou C, Kung MP, Plossl K, Keeney CL, Kung HF: Occupancy of dopamine D2 receptors in the mouse brain measured using ultra-high-resolution single-photon emission tomography and [123]IBF. Eur J Nucl Med Mol Imaging 29:1507-15, 2002a.

Acton PD, Choi SR, Plossl K, Kung HF: Quantification of dopamine transporters in the mouse brain using ultra-high resolution single-photon emission tomography. Eur J Nucl Med Mol Imaging 29:691-8, 2002b.

Acton PD, Thomas D, Zhou R: Quantitative imaging of myocardial infarct in rats with high resolution pinhole SPECT. Int J Cardiovasc Imaging 22:429-34, 2006.

Andringa G, Drukarch B, Bol JG, de Bruin K, Sorman K, Habraken JB, Booij J: Pinhole SPECT imaging of dopamine transporters correlates with dopamine transporter immunohistochemical analysis in the MPTP mouse model of Parkinson's disease. Neuroimage 26:1150-8, 2005.

Anger HO, Rosenthal DJ: Scintillation camera and positron camera. Med Radioisotope Scanning 59–82, 1959.

Arimoto T, Takeishi Y, Fukui A, Tachibana H et al.: Dynamic ^{123}I-MIBG SPECT reflects sympathetic nervous integrity and predicts clinical outcome in patients with chronic heart failure. Annals of Nuclear Medicine 18:145-50, 2004.

Bal G, Acton PD: Analytical derivation of the point spread function for pinhole collimators. Phys Med Biol 51:4923-50, 2006.

Barber DC: The use of principal components in the quantitative analysis of gamma camera dynamic studies. Phys Med Biol 25**:**283–92, 1980.

Beekman FJ, McElroy DP, Berger F, Gambhir SS, Hoffman EJ, Cherry SR: Towards in vivo nuclear microscopy: Iodine-125 imaging in mice using micro-pinholes. Eur J Nucl Med 29:933-938, 2002.

Beekman F J and Vastenhouw B: Design and simulation of a high-resolution stationary SPECT system for small animals. Phys Med Biol 49:4579-92, 2004.

Beekman FJ, van der Have F, Vastenhouw B, van der Linden AJA, van rijk PP, Burbach PH, Smidt MP. USPECT-I: A novel system for submillimeter-resolution tomography with radiolabeled molecules in mice. J Nucl Med 46:1194-1200, 2005.

Beekman F, van der Have F: The pinhole: gateway to ultra-high-resolution three-dimensional radionuclide imaging. Eur J Nucl Med Mol Imaging 34:151-61, 2007.

Beque D, Nuyts J, Bormans G, Suetens P, and Dupont P: Characterization of pinhole SPECT acquisition geometry. IEEE Trans on Med Imag 22:599-612, 2003.

Beque D, Vanhove C, Andreyev A, Nuyts J, and Defrise M: Correction for imperfect camera motion and resolution recovery in pinhole SPECT. Conference Record of 2004 IEEE Medical Imaging Conference (October 16-22, 2004, Rome, Italy), 2004.

Bengel FM, Schwaiger M: Assessment of cardiac sympathetic neuronal function using PET imaging. J Nucl Cardiol 11:603-16, 2004.

Bohlender J, Hildenbrand U, Schlegel W-P, et al: Cardiac function in rats with transgenic, angiotensin IIdependent, hypertension, spontaneously hypertensive rats (SHR) and normotensive controls: a comparative study [in French]. Arch Mal Coeur Vaiss 93:993-996, 2000.

Booij J, de Bruin K, Habraken JB, Voorn P: Imaging of dopamine transporters in rats using high-resolution pinhole single-photon emission tomography. Eur J Nucl Med Mol Imaging 29:1221-4, 2002.

Bristow MR: Mechanism of action of beta-blocking agents in heart failure. Am J Cardiol 80:26L-40L, 1997.

Budinger TF: Advances in the instruments dedicated to imaging single photon radiopharmaceuticals. In Proc of 6th Internal Symp on Technetium in Chemistry and Nuclear Medicine, Sept. 4-7, 2002, Bressanone, Italy, pp. 617-636, 2002.

Carrio I: Cardiac neurotransmission imaging. J Nucl Med 42:1062-76, 2001.

Cherry SR, Gambhir SS: Use of positron emission tomography in animal research. ILAR Journal 42:219-232, 2001.

Constantinesco A, Choquet P, Monassier L, Israel-Jost V, Mertz L: Assessment of left ventricular perfusion, volumes, and motion in mice using pinhole gated SPECT. J Nucl Med 46:1005-1011, 2005.

Crawford CR, Gullberg GT, Tsui BMW: Reconstruction for fan beam with an angular-dependent displaced center-of-rotation. Med Phys 15:67-71, 1988.

Dae MW: Editorial-Scintigraphy of myocardial innervation with metaiodobenzylguanidine (MIBG): Is there a clinical application? J Nucl Cardiol 2:151-4, 1995.

DeGrado TR, Zalutsky MR, Vaidyanathan G: Uptake mechanisms of meta-[^{123}I]iodobenzylguanidine in isolated rat heart. Nucl Med Bio 22:1-12, 1995.

de Win MM, de Jeu RA, de Bruin K, Habraken JB, Reneman L, Booij J, den Heeten GJ: Validity of in vivo [^{123}I]beta-CIT SPECT in detecting MDMA-induced neurotoxicity in rats. Eur Neuropsychopharmacol 14:185-9, 2004.

Dubois EA, Kam KL, Somsen A, et al: Cardiac ^{123}I MIBG uptake in animals with diabetes mellitus and/or hypertension. Eur J Nucl Med 23:901-908, 1996.

Eichhorn EJ, Bristow MRR: Medical therapy can improve the biological properties of the chronically failing heart. Circ 94:2285-2296, 1996.

Esler M, Kaye D, Lambert G, Esler D, Jennings G: Adrenergic nervous system in heart failure. Am J Cardiol 80:7L-14L, 1997.

Forrer F, Valkema R, Bernard B, Schramm NU, Hoppin JW, Rolleman E, Krenning EP, de Jong M: In vivo radionuclide uptake quantification using a multi-pinhole SPECT system to predict renal function in small animals. Eur J Nucl Med Mol Imaging 33:1214-7, 2006.

Furenlid LR, Wilson DW, Chen YC, Kim H, Pietraski PJ, Crawford MJ, Barrett HH. FastSPECT II: A second-generation high-resolution dynamic SPECT imager. IEEE Trans Nucl Sci 51:631-635, 2004.

Gill J, Hunter G, Gane J, Ward D, Camm A: Asymmetry of cardiac ^{123}I meta-iodobenzylguanidine scans in patients with ventricular tachycardia and a "clinically normal" heart. Br Heart J 69:6-13, 1993.

Glowniak JV, Kilty JE, Amara SG, Hoffman BJ, Turner FE: Evaluation of metaiodobenzylguanidine uptake by the norepinephrine, dopamine and serotonin transporters. J Nucl Med 34:1140-1146, 1993.

Goertzen AL, Jones DW, Seidel J, Li K, Green MV: First results from the high-resolution mouse SPECT annular scintillation camera. IEEE Trans Med Imaging 24:863-7, 2005.

Guilloteau D, Baulieu JL, Huguet F, et al: Metaiodobenzylguanidine in adrenal medulla localization: autoradiographic and pharmacologic studies. Eur J Nucl Med 9:278-281, 1984.

Gullberg GT, Tsui BMW, Crawford C, Edgerton E: Estimation of geometrical parameters for fan beam tomography. Phys Med Biol 32:1581-94, 1987.

Habraken JB, de Bruin K, Shehata M, Booij J, Bennink R, van Eck Smit BL, Busemann SE: Evaluation of high-resolution pinhole SPET using a small rotating animal. J Nucl Med 42:1863-1869, 2001.

Hajri T et al.: Defective fatty acid uptake in the spontaneously hypertensive rat is a primary determinant of altered glucose metabolism, hyperinsulinemia, and myocardial hypertrophy. J Biological Chem 276:23661-23666, 2001.

Hesterman JY, Kupinski MA, Furenlid LR, Wilson DW, Barrett HH: The multi-module, multi-resolution system (M3R): a novel small-animal SPECT system. Med Phys 34:987-93, 2007.

Henderson EB, Kahn JK, Corbett JR, Jansen DE et al.: Abnormal I-123 metaiodobenzylguanidine myocardial washout and distribution may reflect myocardial adrenergic derangement in patients with congestive cardiomyopathy. Circulation 78:1192-1199, 1988.

Hirai T, Nohara R, Hosokawa R, Tanaka M, Inada H, Fujibayashi Y, Fujita M, Konishi J, Sasayama S. Evaluation of myocardial infarct size in rat heart by pinhole SPECT. J Nucl Cardiol 7:107-11, 2000.

Hirai T, Nohara R, Ogoh S, Chen LG, Kataoka K, Li XH, Fujita M, Matsumori A, Taguchi S, Sasayama S: Serial evaluation of fatty acid metabolism in rats with myocardial infarction by pinhole SPECT. J Nucl Cardiol 8:472-81, 2001.

Hsieh Y-L: Calibration of Fan Beam Geometry for Single Photon Emission Computed Tomography, M.S. Thesis in Nuclear Engineering, University of Utah, 1992.

Hsu CH, Huang PC: A geometric system model of finite aperture in small animal pinhole SPECT imaging. Comput Med Imaging Graph 30:181-5, 2006.

Huesman RH, Mazoyer BM: Kinetic data analysis with a noisy input function. Phys Med Biol 32:1569-79, 1987.

Ishizu K, Mukai T, Yonekura Y, Pagani M, Fujita T, Magata Y, Nishizawa S, Tamaki N, Shibasaki H, Konishi J: Ultra high resolution SPECT system using four pinhole collimators for small animal studies. J Nucl Med 36:2282-2289, 1995.

Jaszczak RJ, Li J, Wang H, Zalutsky MR, Coleman RE: Pinhole collimation for ultra-high resolution, smallfield-of-view SPECT. Phys Med Biol 39:425-437, 1994.

Kim H, Furenlid LR, Crawford MJ, Wilson DW, Barber HB, Peterson TE, Hunter WC, Liu Z, Woolfenden JM, Barrett HH: SemiSPECT: a small-animal single-photon emission computed tomography (SPECT) imager based on eight cadmium zinc telluride (CZT) detector arrays. Med Phys 33:465-74, 2006.

Kurata C, Uehara A, Ishikawa A: Improvement of cardiac sympathetic innervation by renal transplantation. J Nucl Med 45:1114-20, 2004.

Li J, Jaszczak RJ, Greer KL, Coleman RE: A filtered backprojection algorithm for pinhole SPECT with a displaced center of rotation. Phys Med Biol 39:165-176, 1994.

Li J, Jaszczak RJ, Coleman RE: Quantitative small field-of-view pinhole SPECT imaging: Initial evaluation. IEEE Trans Nucl Sci 42:1109-1113, 1995a.

Li J, Jaszczak R and Coleman E: Maximum likelihood reconstruction for pinhole SPECT with a displaced center-of-rotation. IEEE Trans on Med Imag 14:407-9, 1995b.

Liu Z, Kastis GA, Stevenson GD, Barrett HH, Furenlid LR, Kupinski MA, Patton DD, Wilson DW: Quantitative analysis of acute myocardial infarct in rat hearts with ischemia-reperfusion using a high-resolution stationary SPECT system. J Nucl Med 43:933-9, 2002.

Lotze U, Kaepplinger S, Kober A, Richartz BM, Gottschild D, Figulla HR: Recovery of the cardiac adrenergic nervous system after long-term -blocker therapy in idiopathic dilated

cardiomyopathy: assessment by increase in myocardial ^{123}I-metaiodobenzylguanidine uptake. J Nucl Med 42:49-54, 2001.

MacDonald L, Patt B, Iwanczyk J, et al: Pinhole SPECT of mice using the Lumagem gamma camera. IEEE Trans Nucl Sci 47:1163-1167, 2000.

Massoud TF, Gambhir SS: Molecular imaging in living subjects; seeing fundamental biological processes in a new light. Genes & Development 17:545-580, 2003.

Matsunari I, Bunko H, Taki J, Nakajima K, Muramori A, Kuji I, Miyauchi T, Tonami N, Hisada K: Regional uptake of iodine-125-metaiodobenzylguanidine in the rat heart. Eur J Nucl Med 20:1104-07, 1993.

Maunoury C, Agostini D, Acar P, Antronietti T, Sidi D, Bouvard G, Kachaner J, Barritrault L: Impairment of cardiac neuronal function in childhood dilated cardiomyopathy: an ^{123}I-MIBG scintigraphic study. J Nucl Med 41:400-4, 2000.

McElroy DP, MacDonald LB, Beekman FJ, Wang YC, Patt BE, Iwanczyk JS, Tsui BMW, Hoffman EJ: Performance evaluation of A-SPECT: A high resolution desktop pinhole SPECT system for imaging small animals. IEEE Trans Nucl Sci 49:2139-2147, 2002.

Meikle SR, Kench P, Kassiou M, Banati RB: Small animal SPECT and its place in the matrix of molecular imaging technologies. Phys Med Biol 50:R45-R61, 2005.

Meng LJ, Clinthorne NH: A modified uniform Cramer-Rao bound for multiple pinhole aperture design. IEEE Trans Med Imaging 23:896-902, 2004.

Metzler SD, Bowsher JE, Smith MF, Jaszczak RJ: Analytic determination of pinhole collimator sensitivity with penetration. IEEE Trans on Med Imag 20**:**730–41, 2001.

Metzler S D, Bowsher J E, Greer K L, and Jaszczak R J: Analytic determination of the pinhole collimator's point-spread function and RMS resolution with penetration IEEE Trans Med Imag 21:878 – 87, 2002.

Metzler SD, Geer KL, Jaszczak RJ: Helical pinhole SPECT for small-animal imaging: a method for addressing sampling completeness. IEEE Trans Nucl Sci 50:1575-1583, 2003.

Metzler SD, Greer KL, Bobkov K, Jaszczak RJ: Laser alignment system for helical pinhole SPECT. IEEE Trans Nucl Sci 51:603-610, 2004.

Metzler SD, Jaszczak RJ, Patil NH, Vemulapalli S, Akabani G, Chin BB: Molecular imaging of small animals with a triple-head SPECT system using pinhole collimation. IEEE Trans on Med Imag 24:853–62, 2005a.

Metzler SD, Greer KL, Jaszczak RJ: Determination of mechanical and electronic shifts for pinhole SPECT using a single point source. IEEE Trans on Med Imag 24**:**361-370, 2005b.

Metzler SD, Jaszczak RJ, Greer KL, Bowsher JE: Angular-dependent axial-shift correction for pinhole SPECT. Conference Record of 2005 IEEE Medical Imaging Conference (October 23-29, 2005, Puerto Rico), 2005c.

Mitrani R, Klein L, Miles W, Burt R, Wellman H, Zipes D: Regional cardiac sympathetic denervation in patients with ventricular tachycardia in the absence of coronary artery disease. J Am Coll Cardiol 22:1344-1353, 1993.

Nakajima K, Taki J, Tonami N, and Hisada K: Decreased ^{123}I MIBG uptake and increased clearance in various cardiac diseases. Nucl Med Comm 15:317-23, 1994.

Nakajo M, Shimabukuro K, Yoshimura H, Yonekura R, Nakabeppu Y, Tanoue P, Shinohara S: Iodine-131 metaiodobenzylguanidine intra- and extravesicular accumulation in the rat heart. J Nucl Med 27:84-9, 1986.

Noo F, Clackdoyle R, Mennessier C, White TA, Roney TJ: Analytic method based on identification of ellipse parameters for scanner calibration in cone beam tomography. Phys Med Biol 45:3489–508, 2000.

Ogawa K, Kawade T, Nakamura K, Kubo A, Ichihara T: Ultra high resolution pinhole SPECT for small animal study. IEEE Trans Nucl Sci 45:3122-3126, 1998.

O'Keefe JH, Magaiski A, Stevens TL, Bresnahan DR, Alaswad K, Krueger SK, Bateman TM: Predictors of improvement in left ventricular ejection fraction with carvedilol for congestive heart failure. J Nucl Cardiol 7:3-7, 2000.

Ostendorf B, Scherer A, Wirrwar A, Hoppin JW, Lackas C, Schramm NU, Cohnen M, Mdder U, van den Berg WB, Mller HW, Schneider M, Joosten LA: High-resolution multipinhole single-photon-emission computed tomography in experimental and human arthritis. Arthritis Rheum 54(4):1096-104, 2006.

Palmer J, Wollmer P: Pinhole emission computed tomography: method and experimental evaluation. Phys Med Biol 35:339-50, 1990.

Patel AD, Iskandrian AE: MIBG imaging. J Nucl Cardiol 9:75-94, 2002.

Peremans K, Cornelissen B, Van Den Bossche B, Audenaert K, Van de Wiele C: A review of small animal imaging planar and pinhole SPECT Gamma camera imaging. Vet Radiol Ultrasound 46:162-70, 2005.

Pissarek M, Ermert J, Oesterreich G, Bier D, Coenen HH: Relative uptake, metabolism, and β-receptor binding of (1R,2S)-4-^{18}F-fluorometaraminol and ^{123}I-MIBG in normotensive and spontaneously hypertensive rats. J Nucl Med 43:366-73, 2002.

Press WH, Teukolsky SA, Vetterling WT: Numerical Recipes in C: the Art of Scientific Computing (Cambridge: Cambridge University Press), 1992.

Qi J, Leahy RM, Cherry SR, Chatziioannou A, Farquhar TH: High-resolution 3D Bayesian image reconstruction using the microPET small-animal scanner. Phys Med Biol 43:1001-13, 1998.

Rentmeester MC, van der Have F, Beekman FJ: Optimizing multi-pinhole SPECT geometries using an analytical model. Phys Med Biol 52:2567-81, 2007.

Sato M, Maehara K, Yaoita H, Otani H, Hirosaka A, Saito T, Onuki N, Komatsu N, Ishihata T, Maruyama Y: Correlation between cardiac norepinephrine overflow during exercise and cardiac ^{123}I-MIBG uptake in patients with chronic heart failure. J Nucl Med 44:1618-24, 2003.

Schramm NU, Eberl G, Engeland U, Schurrat T, Behe M, Behr TM: High-resolution SPECT using multipinhole collimation. IEEE Trans Nucl Sci 50:315-320, 2003.

Sisson JC, Wieland DM, Sherman P, Mangner TJ, Tobes MC, Jacques S: Metaiodobenzylguanidine as an index of the adrenergic nervous system integrity and function. J Nucl Med 28:1620-24, 1987.

Sisson JC, Bolgos G, Johnson J: Measuring acute changes in adrenergic nerve activity of the heart in theliving animal. Am Heart J 121:1119-1123, 1991.

Sitek A, Di Bella E V, Gullberg G T: Factor analysis with a priori knowledge--application in dynamic cardiac SPECT. Phys Med Biol 45:2619-38, 2000.

Sitek A, Gullberg GT, Di Bella EV, Celler A: Reconstruction of dynamic renal tomographic data acquired by slow rotation. J Nucl Med 42:1704-12, 2001.

Sitek A, Gullberg GT, Huesman RH: Correction for ambiguous solutions in factor analysis using a penalized least squares objective. IEEE Trans Med Imag 31:216-25, 2002.

Smith MF, Jaszczak RJ, Wang H, Li J: Lead and tungsten pinhole inserts for I-131 SPECT tumor imaging: experimental measurements and photon transport simulations. IEEE Trans Nucl Sci 44:74-82, 1997a.

Smith MF, Jaszczak RJ: The effect of gamma ray penetration on angle-dependent sensitivity for pinhole collimation in nuclear medicine. Med Phys, 24:1701-1709, 1997b.

Smith MF, Jaszczak RJ, Wang H: Pinhole aperture design for I-131 tumor imaging. IEEE Trans Nucl Sci 44:1154-1160, 1997c.

Smith MF, Gilland DR, Coleman RE, Jaszczak RJ: Quantitative imaging of I-131 distributions in brain tumors with pinhole SPECT: A phantom study. J Nucl Med 39:856-864, 1998a.

Smith MF, Jaszczak RJ: An analytic model of pinhole aperture penetration for 3-D pinhole SPECT image reconstruction. Phys Med Biol 43:761-775, 1998b.

Sohlberg A, Lensu S, Jolkkonen J, Tuomisto L, Ruotsalainen U, Kuikka JT: Improving the quality of small animal brain pinhole SPECT imaging by Bayesian reconstruction. Eur J Nucl Med Mol Imaging 31:986-94, 2004.

Strand SE, Ivanovic M, Erlandsson K, Weber DA, Franceschi D, Button T, Sjogreen K: High resolution pinhole SPECT for tumor imaging. Acta Oncol 32(7-8):861-7, 1993.

Strand SE, Ivanovic M, Erlandsson K, Franceschi D, Button T, Sjeogren K, Weber DA: Small animal imaging with pinhole single photon emission computed tomography. Cancer 73:981-984, 1994.

Tenney CR, Smith MF, Greer KL, Jaszczak RJ: Uranium pinhole collimators for I-131 SPECT imaging. IEEE Trans Nucl Sci 46:1165-1171, 1999.

Tomaselli G, Beuckelmann D, Calkins H, et al.: Sudden cardiac death in heart failure - the role of abnormal repolarization. Circ 90:2534-2539, 1994.

Vanhove C, Lahoutte T, Defrise M, Bossuyt A, Franken PR: Reproducibility of left ventricular volume and ejection fraction measurements in rat using pinhole gated SPECT. Eur J Nucl Med Mol Imaging 32:211-220, 2005.

Vastenhouw B, Beekman F: Submillimeter total-body murine imaging with U-SPECT-I. J Nucl Med 48:487-93, 2007.

Wang H, Jaszczak RJ, Coleman RE: Monte Carlo modeling of penetration effect for Iodine-131 pinhole imaging. IEEE Trans Nucl Sci 43:3272-3277, 1996.

Weber DA, Ivanovic M, Franceschi D, Strand SE, Erlandsson K, Franceschi M, Atkins HL, Coderre JA, Susskind H, Button T, et al.: Pinhole SPECT: an approach to in vivo high resolution SPECT imaging in small laboratory animals. J Nucl Med 35:342-348, 1994.

Weber DA, Ivanovic M: Pinhole SPECT: ultra-high resolution imaging for small animal studies. J Nucl Med 36:2287-9, 1995.

Weber DA, Ivanovic M: Ultra-high-resolution imaging of small animals: Implications for preclinical and research studies. J Nucl Cardiol 6:332-334, 1999.

Weissleder R, Mahmod U: Molecular imaging. Radiology 219:316-333, 2001.

Wieland DM, Brown LE, Tobes MC, et al: Imaging the primate adrenal medulla with [^{123}I] and [^{131}I] metaiodobenzylguanidine: Concise communication. J Nucl Med 22:358-364, 1981a.

Wieland DM, Brown LE, Rogers WL et al: Myocardial imaging with a radioiodinated norepinephrine storage analog. J Nucl Med 22:22-31, 1981b.

Wu MC, Tang HR, O'Connell JW, Gao DW, Ido A, Da Silva AJ, Iwata K, Hasegawa BH, Dae MW: An ultra high resolution ECG-gated myocardial imaging system for small animals. IEEE Trans Nucl Sci 46:1199-1202, 1999.

Wu MC, Tang HR, Gao DW, Ido A, O'Connell JW, Hasegawa BH, Dae MW: ECG-gated pinhole SPECT in mice with millimeter spatial resolution. IEEE Trans on Nucl Sci 47:1218-1221, 2000.

Wu M, Gao D, Sievers R, Lee R, Hasegawa B, Dae M: Pinhole single photon emission computed tomography for myocardial perfusion imaging of mice. J Am Coll Cardiol 42:576-582, 2003.

Yokoi T, Iida H, Itoh H, Kanno I: A new graphic plot analysis for cerebral blood flow and partition coefficient with iodine-123-iodoamphetamine and dynamic SPECT validation studies using oxygen-15-water and PET. J Nucl Med 34:498-505, 1993.

Yukihiro M, Inoue T, Iwasaki T, Tomiyoshi K, Erlandsson K, Endo K: Myocardial infarction in rats: high resolution single-photon emission tomographic imaging with a pinhole collimator. Eur J Nucl Med 23:896-900, 1996.

Zeniya T, Watabe H, Aoi T, Kim KM, Teramoto N, Hayashi T, Sohlberg A, Kudo H, Iida H: A new reconstruction strategy for image improvement in pinhole SPECT. Eur J Nucl Med Mol Imaging 31:1166-72, 2004.

Zeniya T, Watabe H, Aoi T, Kim KM, Teramoto N, Takeno T, Ohta Y, Hayashi T, Mashino H, Ota T, Yamamoto S, Iida H: Use of a compact pixellated gamma camera for small animal pinhole SPECT imaging. Ann Nucl Med 20:409-16, 2006.

Zhou R, Thomas DH, Qiao H, Bal HS, Choi SR, Alavi A, Ferrari VA, Kung HF, Acton PD: In vivo detection of stem cells grafted in infarcted rat myocardium. J Nucl Med 46:816-22, 2005.

Zimmerman R, Moore S, Mahmood A: Performance of a triple-detector, multiple-pinhole SPECT system with iodine and indium isotopes. In Nuclear Science Symposium Conference Record, 2004 IEEE vol. 4, pp. 2427-2429.